International Journal of Fracture manuscript No.
(will be inserted by the editor)

Failure mechanisms and fracture energy of hybrid materials

Najam Sheikh, Sivasambu Mahesh

Received: date / Accepted: date

Abstract A shear-lag model of hybrid materials is developed. The model represents an alternating arrangement of two types of aligned linear elastic fibres, embedded in a linear elastic matrix. Fibre and matrix elements are taken to fail deterministically when the axial and shear stresses in them reach their respective strengths. An efficient solution procedure for determining the stress state for arbitrary configurations of broken fibre and matrix elements is developed. Starting with a single fibre break, this procedure is used to simulate progressive fibre and matrix failure, up to composite fracture. The effect of (i) the ratio of fibre stiffnesses, and (ii) the ratio of the fibre tensile strength to matrix shear strength, on the composite failure mechanism, fracture energy, and failure strain is characterised. Experimental observations, reported in the literature, of the fracture behaviour of two hybrid materials, viz., hybrid unidirectional composites, and double network hydrogels, are discussed in the framework of the present model.

1 Introduction

Fibre hybridisation is a well-established methodology to enhance the failure strains of fibre reinforced composites (Hayashi 1972; Bunsell and Harris 1974; Aveston and Sillwood 1976; Zweben 1977; Manders and Bader 1981). In a hybrid composite, the matrix is reinforced by two or more types of fibres, with typically a large stiffness contrast. When exactly two types of fibres are used for reinforcement, the fibres with greater stiffness are conventionally called the low extension (LE) fibres, while those with greater compliance are called high extension (HE) fibres (Fukuda and Chou 1982; Fukunaga et al 1984). Fibre hybridisation can increase both the strain at which the first LE fibre breaks, and the ultimate tensile strain of the composite.

A positive 'hybrid effect' is associated with an increase of the strain at which the first LE fibre breaks over and beyond the strain of first fibre breakage in a composite reinforced only by LE fibres (Swolfs et al 2014). It was long held that the magnitude of this increase may be as much as 50%. However, recent work suggests that this may be an overestimate arising from an error in

Najam Sheikh · Sivasambu Mahesh (✉)

Department of Aerospace Engineering, Indian Institute of Technology Madras, Chennai 600 036, India.

E-mail: smahesh@iitm.ac.in

measuring the baseline strain of first fibre breakage in the equivalent non-hybrid composite (Wisnom et al 2016). The magnitude of the hybrid effect depends on a number of factors (Swolfs et al 2014), including the dispersion of the two fibre types (Hayashi 1972; Bunsell and Harris 1974; Aveston and Sillwood 1976; Zweben 1977; Phillips 1981; Manders and Bader 1981; You et al 2007), the strength of the interface between the fibre types and the matrix (Sharma et al 2014; Kim and Mai 1991; Karger-Kocsis et al 2015), the residual stresses introduced during cooling from a high matrix curing temperature (Bunsell and Harris 1974; Aveston and Sillwood 1976; Zweben 1977; Manders and Bader 1981), and the qualitative differences in the fracture mechanism of the hybrid composite, and its non-hybrid counterpart. The present work is focussed on the last factor. Harlow (1983) proposed that in hybrid composites, cracks produced by the sacrificial failure of LE fibres are bridged and arrested by HE fibres, whereas in the comparable non-hybrid composite, the LE crack runs catastrophically. The larger failure strain of the HE fibres leads to greater ultimate tensile strain of the composite. This explanation suggests a greater hybrid effect for a smaller LE volume fraction, which agrees with experimental observations.

Improvement of the fracture characteristics by hybridisation is not limited to composite materials. Double network hydrogels are water containing polymers synthesised by polymerising the LE monomers in water to form an LE gel (Gong et al 2003). This is followed by swelling the LE gel in a solution of the HE monomer. Despite the multidirectional distribution of polymer strands in double network hydrogels, fracture under uniaxial tension occurs by the failure of polymer strands approximately aligned with the tensile axis. Tsukeshiba et al (2005) reported that the fracture energy of double network hydrogels, comprised of two types of long-chain polymers is about 10^3 times greater than that of the corresponding single network LE or single network HE polymers. Brown (2007) and Tanaka (2007) proposed a model for the fracture toughness enhancement. They hypothesised the formation of a multiply cracked zone ahead of a macroscopic crack, by failure of a number of strands of the LE network. They suggested that this damage, which is mechanically analogous to local yielding at the crack tip, causes shielding of the HE network and increases the fracture energy enormously. This toughening mechanism proposed for double network hydrogels is similar to that proposed by Harlow (1983) for hybrid composites.

Models of the hybrid effect in fibre composites have emphasised the importance of accounting for the randomness of fibre strength. The Weibull (1952) character of the distribution of the fibre strengths is crucial to explaining the enhancement of the ultimate tensile strain of the hybrid composite in the model of Zweben (1977). Fukunaga et al (1984) established the stronger result that models with deterministic fibre strengths cannot predict a positive hybrid effect. In these modelling works, however, only fibre breaks on a plane transverse to the unidirectional fibre direction were considered. Debonding of the fibre matrix interface, or matrix splitting were not represented in these models. However, in experimental fracture studies, especially those wherein the HE reinforcement is glass fibre, extensive failure of the weak interface between glass and epoxy has been reported (Bunsell and Harris 1974; Aveston and Sillwood 1976; Manders and Bader 1981). In double network hydrogels too, damage in the form of LE network breakage extending longitudinally, i.e., parallel to the tensile direction, has been experimentally observed (Yu et al 2009).

In the present work, a one-dimensional shear-lag model (Cox 1952; Hedgepeth 1961) of a hybrid material is proposed, which accounts not only for fibre breakage, but also for matrix splitting or interfacial debonding. An efficient computational solution of this model is proposed by extending the eigenvector expansion method of Fukunaga et al (1984). Composite failure simulations that allow both fibre and matrix failure are performed. The fibres fail by breaking when the axial stress in them exceeds a deterministic critical strength. Similarly, matrix elements split or interfacial elements debond when their shear stress exceeds their deterministic strength. It is shown that a positive hybrid effect is possible when matrix splitting or debonding events are accounted for, even in a hybrid composite with deterministic fibre and matrix/interfacial strengths. Although the energy release during matrix failure is small, it is found that matrix failure alters the development of fibre breaks, which in turn, increases the fracture energy.

The effect of the (i) stiffness contrast of the constituent phases, and (ii) strength contrast between the fibres and the matrix/interface, on the fracture energy, fracture load, and fracture strain, are then systematically elucidated through the simulations. This permits the identification of stiffness and strength contrasts that produce the greatest fracture energy, greatest hybrid effect, and greatest ultimate tensile strain, along with the corresponding failure mechanisms. It is found that the optimal stiffness and strength contrasts to maximise the fracture energy, and ultimate tensile strain, are quite similar, but quite different from that needed to maximise the hybrid effect. High strength and stiffness contrasts are needed for the former, while much smaller stiffness and strength contrasts are needed for the latter.

2 Model

2.1 Elastostatic fields in the model composite lamina

Consider a composite lamina composed of a homogeneous linear elastic matrix reinforced unidirectionally by two types of infinitely long, linear elastic fibres, as shown in Fig. 1. The stiff and compliant fibre types alternate as shown, and are designated LE and HE types, respectively, following convention. Let there be N LE and N HE fibres. Fibres f_{2i-1}, and f_{2i}, are the LE and HE fibres, respectively, for $i \in \{1, 2, \dots, N\}$. The set of all LE fibres, and HE fibres are denoted $\mathscr{L}$ and $\mathscr{H}$, respectively:

$$\begin{aligned} \mathscr{L} &= \left\{ f_{2i-1} \,:\, i \in \{1, 2, \dots, N\} \right\}, \text{ and} \\ \mathscr{H} &= \left\{ f_{2i} \,:\, i \in \{1, 2, \dots, N\} \right\}. \end{aligned} \tag{1}$$

The composite lamina is assumed periodic in the transverse direction, so that the two neighbours of fibre f_i, $i \in \{1, 2, \dots, 2N\}$ are the fibres $f_{[i\pm1]}$, where,

$$[i] = i - 2N \left\lfloor \frac{i-1}{2N} \right\rfloor. \tag{2}$$

Here, $\lfloor \cdot \rfloor$ denotes the largest integer no greater than its argument. A matrix bay intervenes between two adjacent fibres. The matrix bay between fibres f_i and $f_{[i+1]}$ is denoted m_i. The nomenclature of the fibres and matrix in an $N = 3$ composite lamina is shown in Fig. 1. Also, as shown, the longitudinal and transverse directions in the composite lamina are denoted x, and y, respectively.

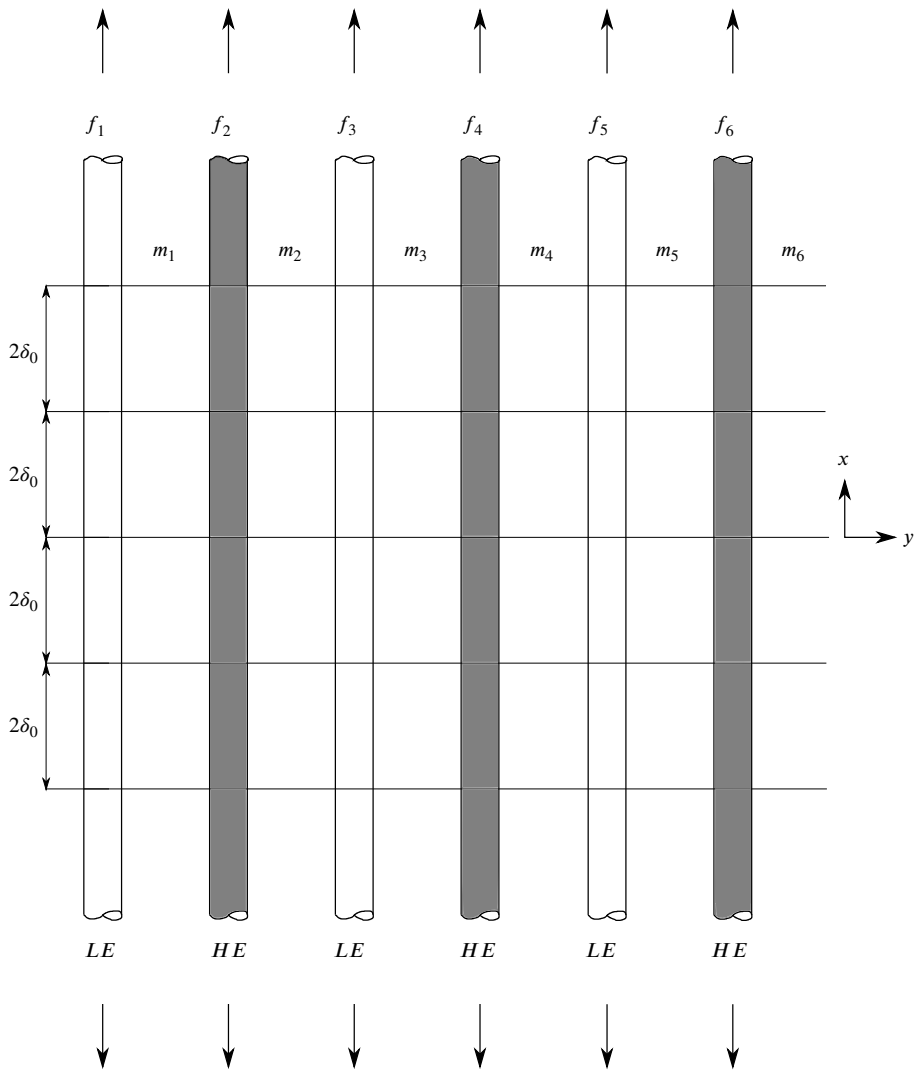

Fig. 1: Schematic hybrid composite reinforced by $N = 3$ LE fibres, and $N = 3$ HE fibres. The fibre and matrix bay numbering scheme is illustrated. Periodicity is assumed so that the right-most and left-most fibres are neighbours. The schematic also shows the conceptual longitudinal sectioning of the composite into mechanically independent 'layers', each of length $2\delta_0$.

Following the standard shear-lag assumptions (Cox 1952; Hedgepeth 1961), both LE and HE fibre elements are taken to be loaded in uniaxial tension, and the matrix elements in simple shear. That is, it is assumed that σ_{xx} is the only non-zero stress component in the fibres, and σ_{xy} is the only non-zero stress in the matrix. All phases are assumed linear elastic.

Let $u_{f_i}(x)$ denote the axial, i.e., x-directional displacement of fibre f_i at position x. Then, the axial strain at that location is given by

$$\epsilon_{f_i}(x) = \frac{du_{f_i}}{dx}(x). \tag{3}$$

The extensional stiffness of a fibre is a product of its Youngs modulus, E, and its cross-sectional area, A. Let $k_{\mathrm{LE}} = (EA)_{\mathrm{LE}}$ and $k_{\mathrm{HE}} = (EA)_{\mathrm{HE}}$ denote the extensional stiffnesses of the LE and HE fibres, respectively. The assumption that

$$k_{\mathrm{HE}} \leq k_{\mathrm{LE}} \tag{4}$$

is consistent with the present terminology. The load carried by the LE and HE fibres are

$$p_{f_i}(x) = \begin{cases} k_{\mathrm{LE}} \frac{du_{f_i}}{dx}(x), & \text{if } f_i \in \mathscr{L}, \\ k_{\mathrm{HE}} \frac{du_{f_i}}{dx}(x), & \text{if } f_i \in \mathscr{H}. \end{cases} \tag{5}$$

The shear strain in matrix bay m_i is given by

$$\gamma_{m_i}(x) = \frac{u_{f_{[i+1]}}(x) - u_{f_i}(x)}{w}, \tag{6}$$

where w is the width of the matrix bay. If G is the matrix shear modulus, the corresponding shear stress is given by $\tau_{f_i}(x) = G\gamma_{f_i}(x)$. Assuming both LE and HE fibres have the same diameter d, and defining

$$S = Gd/w, \tag{7}$$

the shear flow in matrix bay m_i is:

$$q_{m_i}(x) = S(u_{f_{[i+1]}}(x) - u_{f_i}(x)). \tag{8}$$

2.2 Undamaged model composite lamina

Consider an undamaged model hybrid composite, as shown in Fig. 1. Let k_0 be a reference fibre stiffness. Let the far-field tensile load applied on the composite be $N(k_{\mathrm{HE}}/k_0 + k_{\mathrm{LE}}/k_0)p_\infty$. In the special case that the fibre stiffnesses coincide, i.e., $k_{\mathrm{LE}} = k_{\mathrm{HE}} = k_0$, the total load applied on the composite is $2Np_\infty$, and p_∞ then denotes the applied load per fibre. The composite strain is then given by p_∞/k_0.

Let the fibre strains in the general case that $k_{\mathrm{LE}} \neq k_{\mathrm{HE}}$ also be

$$\frac{du^0_{f_i}}{dx}(x) = \frac{p_\infty}{k_0}, \quad \text{for all } i \in \mathscr{L} \cup \mathscr{H}. \tag{9}$$

The superscript '0' identifies the undamaged state. The loads carried by the LE and HE fibres are now obtained by substituting Eq. (9) into Eq. (5):

$$p^0_{f_i}(x) = \begin{cases} \frac{k_{\mathrm{LE}}}{k_0} p_\infty, & \text{if } f_i \in \mathscr{L}, \\ \frac{k_{\mathrm{HE}}}{k_0} p_\infty, & \text{if } f_i \in \mathscr{H}. \end{cases} \tag{10}$$

Furthermore,

$$\sum_{i=1}^{2N} p^0_{f_i}(x) = N(k_{\mathrm{HE}}/k_0 + k_{\mathrm{LE}}/k_0)p_\infty, \tag{11}$$

i.e., the resultant of the fibre loads equals the load applied to the composite. It follows that $du^0_{f_i}(x)/dx$ and $p^0_{f_i}(x)$ given by Eqs. (9) and (10) are indeed the strains and loads in fibres of the undamaged hybrid composite.

Fixing the fibre displacements at $x = 0$, i.e., fixing $u^0_{f_i}(x = 0) = 0$, Eq. (9) yields

$$u^0_{f_i}(x) = \frac{p_\infty}{k_0} x, \quad \text{for all } f_i \in \mathscr{L} \cup \mathscr{H}. \tag{12}$$

Since the fibre displacements, $u^0_{f_i}(x)$, are equal for all $f_i \in \mathscr{L} \cup \mathscr{H}$, by Eq. (8),

$$q^0_{m_i}(x) = 0, \text{ for all } i \in \{1, 2, \ldots, 2N\}. \tag{13}$$

2.3 Discretisation of the model composite lamina into 'blocks'

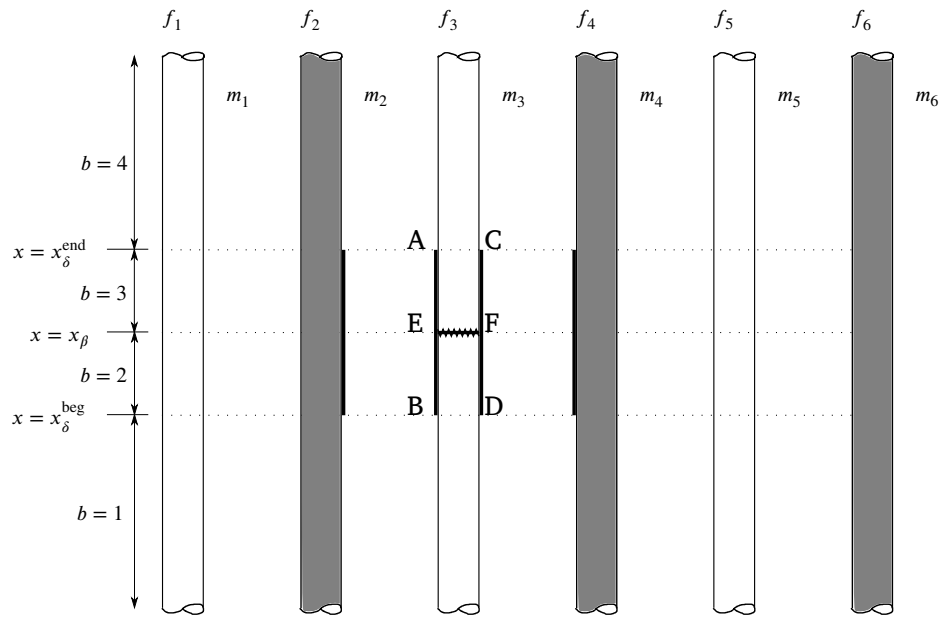

(a) One broken fibre, f_3, and adjacent matrix failure.

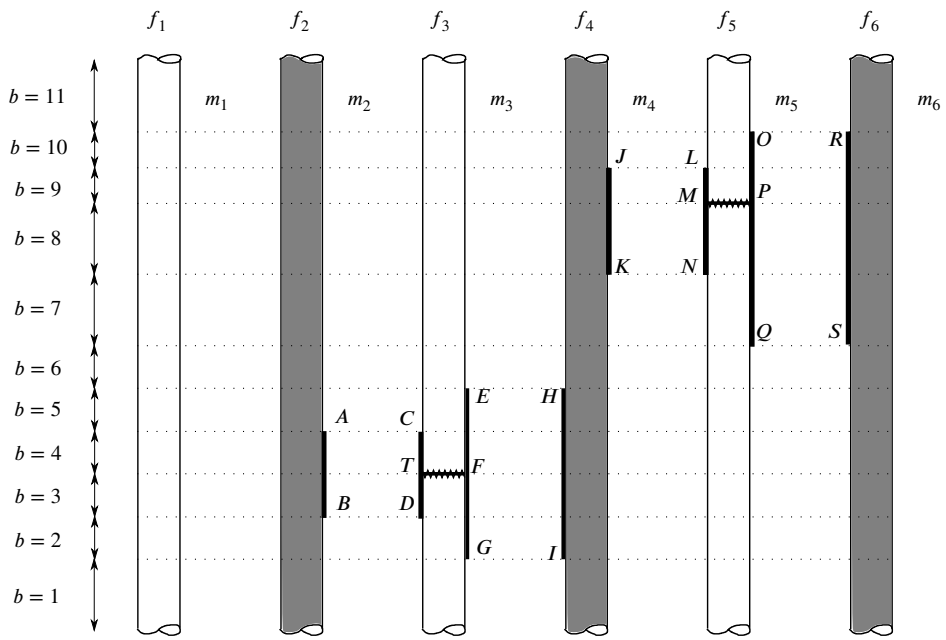

(b) Two broken fibres, f_3 and f_5, and adjacent matrix failure.

Fig. 2: (a) Simple and (b) more complex arrangement of breaks and matrix failure in an $N = 3$ hybrid composite comprised of 3 LE and 3 HE fibres. (a) and (b) are discretised using 4 and 11 blocks, respectively.

Next, a composite lamina with arbitrarily located fibre breaks, and matrix failures is considered. Two examples, for $N = 3$ laminae, comprised of 3 LE and 3 HE fibres, are shown in Fig. 2. Let the β-th fibre break occur in fibre f_{F_β} at axial position, x_β, and let the δ-th matrix failure occur in the matrix bay m_{M_δ}, and extend between $x \in (x_\delta^{\text{beg}}, x_\delta^{\text{end}})$. The fibre breaks, and matrix failures are introduced prior to loading. The mechanical effect of the matrix failure is to annul the shear flow over its length, i.e.,

$$q_{m_{M_\delta}}(x) = 0, \text{ for } x \in (x_\delta^{\text{beg}}, x_\delta^{\text{end}}). \tag{14}$$

The mechanical consequence given by Eq. (14) can be achieved either by debonding (i) the LE fibre/matrix interfaces, or (ii) the HE fibre/matrix interfaces, or (iii) both. It can also be obtained by (iv) splitting (Goree and Gross 1980; Dharani and Recker 1991) the matrix bay, m_{M_δ}. Although the sketches in Fig. 2 indicate debonding at both interfaces of the matrix bays, it is emphasised that all the four causes listed above have an equivalent mechanical effect insofar as the boundary value problem is concerned. Henceforth, the specific physical failure events leading to the mechanical consequence $q_{m_i} = 0$ are not distinguished. Any physical failure event that results in $q_{m_{M_\delta}} = 0$ is termed 'matrix failure' in matrix bay m_{M_δ}.

For the purpose of analysis, block boundaries are constructed at the axial coordinate of each fibre break, x_β, and at the beginning and end of each matrix failure, x_δ^{beg}, and x_δ^{end}, as shown in Fig. 2b. If this procedure results in coincident block boundaries, duplicates are eliminated. Let the number of block boundaries so formed be B. When arranged in ascending order, let the block boundaries be located at $x^{(1)} < x^{(2)} < \ldots < x^{(B)}$. It is convenient to define $x^{(0)} = -\infty$, and $x^{(B+1)} = \infty$. Block b extends over $x \in (x^{(b-1)}, x^{(b)})$. By construction, fibre breaks are located at the block boundaries, and matrix failures initiate and terminate at block boundaries. As shown, the fibre breaks and matrix failures in Figs. 2a, and 2b require 4, and 11 blocks for discretising, respectively.

Let

$$\mathscr{B}^{(b)} = \{\beta : x_\beta = x^{(b)}\} \tag{15}$$

denote the set of all fibre breaks at the b-th block boundary, i.e., at the interface between blocks (b) and $(b+1)$. Similarly, let

$$\mathscr{D}^{(b)} = \{\delta : x_\delta^{\text{beg}} = x^{(b-1)}, \text{ and } x_\delta^{\text{end}} = x^{(b)}\} \tag{16}$$

denote the set of all matrix failures contained in the b-th block. The indicator function,

$$1_{m_i}^{(b)} = \begin{cases} 1, & \text{if } i \neq M_\delta, \text{ for all } \delta \in \mathscr{D}^{(b)}, \\ 0, & \text{if } i = M_\delta, \text{ for any } \delta \in \mathscr{D}^{(b)}, \end{cases} \tag{17}$$

indicates failure or otherwise of matrix bay m_i in block (b).

2.4 Boundary value problem

Let $u^{(b)}_{f_i}(x)$ be a twice differentiable function, and denote the displacement field in fibre f_i over the domain of block (b). Let $q^{(b)}_{m_i}(x)$ denote the shear flow in matrix bay, m_i, in block (b). The shear flow and fibre displacements are related through Eq. (8):

$$q^{(b)}_{m_i}(x) = S\left(u^{(b)}_{f_{[i+1]}}(x) - u^{(b)}_{f_i}(x)\right)1^{(b)}_{m_i}. \tag{18}$$

Eq. (18) gives zero shear flow in failed matrix bays ($1^{(b)}_{m_i} = 0$).

Following Hedgepeth (1961), Fukuda and Chou (1982), and Fukunaga et al (1984), the equations governing the fibre displacements are statements of equilibrium of infinitesimal fibre segments:

$$\begin{aligned} k_{\mathrm{LE}}\frac{d^2u^{(b)}_{f_i}}{dx^2}(x) + q^{(b)}_{m_{[i-1]}} + q^{(b)}_{m_i} = 0, \text{ if } f_i \in \mathscr{L}, \text{ and} \\ k_{\mathrm{HE}}\frac{d^2u^{(b)}_{f_i}}{dx^2}(x) + q^{(b)}_{m_{[i-1]}} + q^{(b)}_{m_i} = 0, \text{ if } f_i \in \mathscr{H}. \end{aligned} \tag{19}$$

Substituting Eq. (18) into Eq. (19) yields:

$$\begin{aligned} k_{\mathrm{LE}}\frac{d^2u^{(b)}_{f_i}}{dx^2}(x) + S\left(u^{(b)}_{f_{[i+1]}}(x)1^{(b)}_{m_i} + u^{(b)}_{f_{[i-1]}}(x)1^{(b)}_{m_{[i-1]}} - \left(1^{(b)}_{m_i} + 1^{(b)}_{m_{[i-1]}}\right)u^{(b)}_{f_i}(x)\right) = 0, \text{ if } f_i \in \mathscr{L} \text{ and} \\ k_{\mathrm{HE}}\frac{d^2u^{(b)}_{f_i}}{dx^2}(x) + S\left(u^{(b)}_{f_{[i+1]}}(x)1^{(b)}_{m_i} + u^{(b)}_{f_{[i-1]}}(x)1^{(b)}_{m_{[i-1]}} - \left(1^{(b)}_{m_i} + 1^{(b)}_{m_{[i-1]}}\right)u^{(b)}_{f_i}(x)\right) = 0, \text{ if } f_i \in \mathscr{H}, \end{aligned} \tag{20}$$

for all $x \in (x^{(b-1)}, x^{(b)})$, excluding the end points. The square brackets around some subscripts indicate that they must be wrapped around periodically, as specified in Eq. (2).

Let $\{u^{(b)}(x)\} = \left\{u^{(b)}_1(x), u^{(b)}_2(x), \ldots, u^{(b)}_{2N}(x)\right\}^T$ denote a column vector of displacement functions in block (b). Following Fukunaga et al (1984), and Landis et al (2000), consider the $2N \times 2N$ matrix $[a^{(b)}]$, whose elements are zero, except for:

$$a^{(b)}_{i,[i+1]} = \begin{cases} \frac{S}{k_{\mathrm{LE}}}1^{(b)}_{m_i}, & \text{if } f_i \in \mathscr{L}, \\ \frac{S}{k_{\mathrm{HE}}}1^{(b)}_{m_i}, & \text{if } f_i \in \mathscr{H}, \end{cases} \tag{21}$$

$$a^{(b)}_{[i+1],i} = \begin{cases} \frac{S}{k_{\mathrm{LE}}}1^{(b)}_{m_i}, & \text{if } f_{[i+1]} \in \mathscr{L}, \\ \frac{S}{k_{\mathrm{HE}}}1^{(b)}_{m_i}, & \text{if } f_{[i+1]} \in \mathscr{H}, \end{cases} \tag{22}$$

and diagonal elements $a^{(b)}_{ii}$ given by

$$a^{(b)}_{ii} = -a^{(b)}_{i,[i-1]} - a^{(b)}_{i,[i+1]}. \tag{23}$$

For example, the matrices $[a^{(1)}]$, and $[a^{(B+1)}]$ corresponding to the infinitely long end blocks in Fig. 2 are:

$$[a^{(1)}] = [a^{(B+1)}] = S\begin{pmatrix} -2/k_{\mathrm{LE}} & 1/k_{\mathrm{LE}} & 0 & 0 & 0 & 1/k_{\mathrm{LE}} \\ 1/k_{\mathrm{HE}} & -2/k_{\mathrm{HE}} & 1/k_{\mathrm{HE}} & 0 & 0 & 0 \\ 0 & 1/k_{\mathrm{LE}} & -2/k_{\mathrm{LE}} & 1/k_{\mathrm{LE}} & 0 & 0 \\ 0 & 0 & 1/k_{\mathrm{HE}} & -2/k_{\mathrm{HE}} & 1/k_{\mathrm{HE}} & 0 \\ 0 & 0 & 0 & 1/k_{\mathrm{LE}} & -2/k_{\mathrm{LE}} & 1/k_{\mathrm{LE}} \\ 1/k_{\mathrm{HE}} & 0 & 0 & 0 & 1/k_{\mathrm{HE}} & -2/k_{\mathrm{HE}} \end{pmatrix}. \tag{24}$$

As another example, the matrices $[a^{(2)}]$ and $[a^{(3)}]$ in Fig. 2a or matrices $[a^{(3)}]$ and $[a^{(4)}]$ in Fig. 2b are all equal to:

$$S\begin{pmatrix} -2/k_{\mathrm{LE}} & 1/k_{\mathrm{LE}} & 0 & 0 & 0 & 1/k_{\mathrm{LE}} \\ 1/k_{\mathrm{HE}} & -1/k_{\mathrm{HE}} & 0 & 0 & 0 & 0 \\ 0 & 0 & 0 & 0 & 0 & 0 \\ 0 & 0 & 0 & -1/k_{\mathrm{HE}} & 1/k_{\mathrm{HE}} & 0 \\ 0 & 0 & 0 & 1/k_{\mathrm{LE}} & -2/k_{\mathrm{LE}} & 1/k_{\mathrm{LE}} \\ 1/k_{\mathrm{HE}} & 0 & 0 & 0 & 1/k_{\mathrm{HE}} & -2/k_{\mathrm{HE}} \end{pmatrix}. \tag{25}$$

In terms of $[a^{(b)}]$, the governing differential equations, Eq. (20), can be expressed as:

$$\frac{d^2\{u^{(b)}(x)\}}{dx^2} + [a^{(b)}]\{u^{(b)}(x)\} = \{0\}, \text{ for } x \in (x^{(b-1)}, x^{(b)}). \tag{26}$$

Comparing Eqs. (26) and (19), it is clear that

$$[a^{(b)}]\{u^{(b)}(x)\} = \{q_{m_{[i-1]}}(x) + q_{m_i}(x)\}. \tag{27}$$

Displacement and traction continuity are required across block boundary b, delineating blocks (b), and $(b+1)$, in all intact fibres. These are:

$$u^{(b)}_{f_i}(x = x^{(b)}) = u^{(b+1)}_{f_i}(x = x^{(b)}), \text{ if } i \neq F_\beta, \text{ for all } \beta \in \mathscr{B}^{(b)}, \tag{28}$$

and

$$\frac{du^{(b)}_{f_i}}{dx}(x = x^{(b)}) = \frac{du^{(b+1)}_{f_i}}{dx}(x = x^{(b)}), \text{ if } i \neq F_\beta, \text{ for all } \beta \in \mathscr{B}^{(b)}, \tag{29}$$

respectively. At fibre breaks located in block boundary b, traction free boundary conditions:

$$\frac{du^{(b)}_{f_i}}{dx}(x = x^{(b)}) = \frac{du^{(b+1)}_{f_i}}{dx}(x = x^{(b)}) = 0, \text{ if } i = F_\beta, \text{ for any } \beta \in \mathscr{B}^{(b)}, \tag{30}$$

are imposed. The far-field boundary conditions imposed on blocks $b = 1$, and $b = B + 1$ are:

$$\frac{du^{(1)}_{f_i}}{dx}(x = -\infty) = \frac{du^{(B+1)}_{f_i}}{dx}(x = \infty) = \frac{p_\infty}{k_0}, \tag{31}$$

which corresponds to a total far-field applied load of $N(k_{\mathrm{HE}}/k_0 + k_{\mathrm{LE}}/k_0)p_\infty$.

2.5 Non-dimensional auxiliary boundary value problem

Following Beyerlein et al (1996), let the fibre displacements be decomposed into a homogeneous part, $u^0_{f_i}(x)$, due to the far-field loading, and a part $\tilde{u}^{(b)}_{f_i}(x)$ due to the fibre breaks and matrix failures:

$$u^{(b)}_{f_i}(x) = u^0_{f_i}(x) + \tilde{u}^{(b)}_{f_i}(x). \tag{32}$$

$u^0_{f_i}(x)$ is given by Eq. (12). Substituting Eq. (32) into Eq. (26), and noting from Eqs. (27) and (13) that $[a^{(b)}]\{u^0_{f_i}\} = \{0\}$, it is seen that

$$\frac{d^2\{\tilde{u}^{(b)}(x)\}}{dx^2} + [a^{(b)}]\{\tilde{u}^{(b)}(x)\} = \{0\}, \text{ for } x \in (x^{(b-1)}, x^{(b)}), \tag{33}$$

which is termed the governing equation of the 'auxiliary problem' (Beyerlein et al 1996). The foregoing equation is considerably simplified when non-dimensionalised, following Hedgepeth (1961). The axial coordinate is normalised as

$$\xi = \frac{x}{\sqrt{k_0/S}}. \tag{34}$$

The normalised auxiliary fibre displacements are defined as

$$\tilde{U}^{(b)}_{f_i} = \begin{cases} \tilde{u}^{(b)}_{f_i}\sqrt{k_{\mathrm{LE}}S}/p_\infty, & \text{if } f_i \in \mathscr{L}, \text{ and} \\ \tilde{u}^{(b)}_{f_i}\sqrt{k_{\mathrm{HE}}S}/p_\infty, & \text{if } f_i \in \mathscr{H}. \end{cases} \tag{35}$$

Let $\{\tilde{U}^{(b)}(\xi)\} = \left\{\tilde{U}^{(b)}_1(\xi), \tilde{U}^{(b)}_2(\xi), \ldots, \tilde{U}^{(b)}_{2N}(\xi)\right\}^T$ denote the column vector of non-dimensional auxiliary displacements of the fibres in block (b). Let

$$\eta_{\mathrm{LE}} = k_{\mathrm{LE}}/k_0, \quad \text{and} \quad \eta_{\mathrm{HE}} = k_{\mathrm{HE}}/k_0. \tag{36}$$

Then, changing variables from x, and $\{\tilde{u}^{(b)}(x)\}$ in Eq. (33) to ξ, and $\{\tilde{U}^{(b)}(\xi)\}$, respectively, yields

$$\frac{d^2\{\tilde{U}^{(b)}(\xi)\}}{d\xi^2} + [A^{(b)}]\{\tilde{U}^{(b)}(\xi)\} = \{0\}, \tag{37}$$

where,

$$A^{(b)}_{i,[i+1]} = A^{(b)}_{[i+1],i} = \frac{1}{\sqrt{\eta_{\mathrm{LE}}\eta_{\mathrm{HE}}}}, \tag{38}$$

All other off-diagonal elements of $[A^{(b)}]$ are zero. The diagonal elements are given by

$$A^{(b)}_{ii} = \begin{cases} -\frac{2}{\eta_{\mathrm{LE}}}, & \text{if } f_i \in \mathscr{L}, \text{ and} \\ -\frac{2}{\eta_{\mathrm{HE}}}, & \text{if } f_i \in \mathscr{H}. \end{cases} \tag{39}$$

$[A^{(b)}]$ is symmetric and negative semi-definite (Fukunaga et al 1984).

It is recalled that $\mathscr{B}^{(b)}$ denotes the set of fibre breaks at block boundary b, between blocks (b) and $(b+1)$. Expressed in terms of the non-dimensional ξ, let the block boundaries be located at $\xi^{(1)}, \xi^{(2)}, \ldots, \xi^{(B)}$, where using Eq. (34):

$$\xi^{(b)} = \frac{x^{(b)}}{\sqrt{k_0/S}}. \tag{40}$$

The non-dimensional continuity conditions at block boundary b for the auxiliary displacement fields are obtained from Eqs. (28) and (29), using Eqs. (32), and (35) as:

$$\tilde{U}^{(b)}_{f_i}(\xi = \xi^{(b)}) = \tilde{U}^{(b+1)}_{f_i}(\xi = \xi^{(b)}), \text{ if } i \neq F_\beta, \text{ for all } \beta \in \mathscr{B}^{(b)}, \tag{41}$$

and

$$\frac{d\tilde{U}_{f_i}^{(b)}}{d\xi}(\xi=\xi^{(b)}) = \frac{d\tilde{U}_{f_i}^{(b+1)}}{d\xi}(\xi=\xi^{(b)}), \text{ if } i \neq F_\beta, \text{ for all } \beta \in \mathscr{B}^{(b)}, \tag{42}$$

respectively. The traction free boundary conditions, Eq. (42) become:

$$\frac{d\tilde{U}_{f_i}^{(b)}}{d\xi}(\xi=\xi^{(b)}) = \frac{d\tilde{U}_{f_i}^{(b+1)}}{d\xi}(\xi=\xi^{(b)}) = \begin{cases} -\sqrt{\eta_{\mathrm{LE}}}, & \text{if } f_i \in \mathscr{L}, \text{ and} \\ -\sqrt{\eta_{\mathrm{HE}}}, & \text{if } f_i \in \mathscr{H}, \end{cases} \tag{43}$$

if $i = F_\beta$, for any $\beta \in \mathscr{B}^{(b)}$. Finally the normalised auxiliary far-field boundary conditions imposed in blocks $b = 1$, and $b = B+1$ become:

$$\frac{d\tilde{U}_{f_i}^{(1)}}{d\xi}(\xi=-\infty) = \frac{d\tilde{U}_{f_i}^{(B+1)}}{d\xi}(\xi=\infty) = 0, \tag{44}$$

for all $f_i \in \mathscr{L} \cup \mathscr{H}$.

2.6 Normalised strains and loads

Let $E_{f_i}^0$ and $P_{f_i}^0$ represent the normalised strains and loads in fibre f_i in an undamaged composite. Substituting Eqs. (34) and (35) into Eq. (9) yields

$$E_{f_i}^0(\xi) = \frac{dU_{f_i}}{d\xi}(\xi) = \begin{cases} \sqrt{\eta_{\mathrm{LE}}} & \text{if } f_i \in \mathscr{L}, \text{ and} \\ \sqrt{\eta_{\mathrm{HE}}} & \text{if } f_i \in \mathscr{H}. \end{cases} \tag{45}$$

Also, the normalised load in fibre f_i in an undamaged composite is defined as:

$$P_{f_i}^0 = \frac{p_{f_i}^0}{p_\infty} = \begin{cases} \eta_{\mathrm{LE}}, & \text{if } f_i \in \mathscr{L}, \\ \eta_{\mathrm{HE}}, & \text{if } f_i \in \mathscr{H}. \end{cases} \tag{46}$$

Let $\tilde{E}_{f_i}^{(b)}(x)$, and $\tilde{P}_{f_i}^{(b)}(x)$ represent the auxiliary normalised strain and normalised load in fibre f_i in block (b). They are defined as:

$$\begin{aligned} \tilde{E}_{f_i}^{(b)}(\xi) &= \begin{cases} \frac{\epsilon_i^{(b)}}{(p_\infty/\sqrt{k_{\mathrm{LE}}k_0})}, & \text{if } f_i \in \mathscr{L}, \text{ and} \\ \frac{\epsilon_i^{(b)}}{(p_\infty/\sqrt{k_{\mathrm{HE}}k_0})}, & \text{if } f_i \in \mathscr{H}, \end{cases} \\ &= \frac{d\tilde{U}_i^{(b)}}{d\xi}(\xi), \end{aligned} \tag{47}$$

and

$$\tilde{P}_{f_i}^{(b)}(\xi) = \frac{\tilde{p}_{f_i}^{(b)}}{p_\infty} = \begin{cases} \sqrt{\eta_{\mathrm{LE}}}\,\frac{d\tilde{U}_{f_i}^{(b)}}{d\xi}(\xi), & \text{if } f_i \in \mathscr{L}, \text{ and} \\ \sqrt{\eta_{\mathrm{HE}}}\,\frac{d\tilde{U}_{f_i}^{(b)}}{d\xi}(\xi), & \text{if } f_i \in \mathscr{H}, \end{cases} \tag{48}$$

respectively. The normalised load in fibre f_i, $P^{(b)}_{f_i}$ is simply the sum of the normalised load from the auxiliary problem, and that due to the far-field loads, $P^0_{f_i}$, defined in Eq. (46):

$$P^{(b)}_{f_i}(\xi) = P^0_{f_i}(\xi) + \tilde{P}^{(b)}_{f_i}(\xi). \tag{49}$$

Similarly, the normalised strain can be obtained using superposition as:

$$E^{(b)}_{f_i}(\xi) = E^0_{f_i}(\xi) + \tilde{E}^{(b)}_{f_i}(\xi). \tag{50}$$

The normalised shear strain and shear stress, $\Gamma^{(b)}_{m_i}$, and $T^{(b)}_{m_i}$ in matrix bay m_i are defined as:

$$\Gamma^{(b)}_{m_i}(\xi) = \frac{\gamma^{(b)}_{m_i}}{(p_\infty/w\sqrt{Sk_0})} = \begin{cases} \frac{\tilde{U}^{(b)}_{f_{[i+1]}}(\xi)}{\sqrt{\eta_{\mathrm{HE}}}} - \frac{\tilde{U}^{(b)}_{f_i}(\xi)}{\sqrt{\eta_{\mathrm{LE}}}}, & \text{if } f_i \in \mathscr{L} \text{ and,} \\ \frac{\tilde{U}^{(b)}_{f_{[i+1]}}(\xi)}{\sqrt{\eta_{\mathrm{LE}}}} - \frac{\tilde{U}^{(b)}_{f_i}(\xi)}{\sqrt{\eta_{\mathrm{HE}}}}, & \text{if } f_i \in \mathscr{H}, \end{cases} \tag{51}$$

and,

$$T^{(b)}_{m_i}(\xi) = \frac{\tau^{(b)}_i}{(Gp_\infty/w\sqrt{Sk_0})} = \begin{cases} \frac{\tilde{U}^{(b)}_{f_{[i+1]}}(\xi)}{\sqrt{\eta_{\mathrm{HE}}}} - \frac{\tilde{U}^{(b)}_{f_i}(\xi)}{\sqrt{\eta_{\mathrm{LE}}}}, & \text{if } f_i \in \mathscr{L}, \text{ and,} \\ \frac{\tilde{U}^{(b)}_{f_{[i+1]}}(\xi)}{\sqrt{\eta_{\mathrm{LE}}}} - \frac{\tilde{U}^{(b)}_{f_i}(\xi)}{\sqrt{\eta_{\mathrm{HE}}}}, & \text{if } f_i \in \mathscr{H}, \end{cases} \tag{52}$$

respectively. Since the shear strains and stresses in the undamaged composite are zero, the total and auxiliary shear strains and stresses are eqaul. $\Gamma^{(b)}_{m_i}(\xi)$, and $T^{(b)}_{m_i}(\xi)$ represent both the auxiliary and total normalised quantitites.

2.7 Solution of the auxiliary boundary value problem

The present solution methodology extends the eigenvector method proposed by Fukunaga et al (1984), and Landis et al (2000), by allowing for arbitrary axial locations of fibre breaks, and arbitrary matrix failures in the composite lamina.

Let $\{C^{(b)}_\imath\}$, for $\imath \in \{1, 2, \dots, 2N\}$ be the $2N$ unit eigenvectors of the matrix $[A^{(b)}]$ corresponding to eigenvalues $\lambda^{(b)}_\imath$. $[A^{(b)}]$ is symmetric and negative semi-definite. Therefore,

$$\lambda^{(b)}_\imath \leq 0, \quad \text{for } \imath \in \{1, 2, \dots, 2N\}. \tag{53}$$

Following Mahesh and Phoenix (2004), a solution of the governing Eq. (37) of the form:

$$\{\tilde{U}^{(b)}(\xi)\} = \sum_{\imath=1}^{2N} \left\{C^{(b)}_\imath\right\} \left[\phi^{(b)}_\imath \exp(-\lambda^{(b)}_\imath \xi) - \psi^{(b)}_\imath \exp(+\lambda^{(b)}_\imath \xi)\right], \tag{54}$$

for each block $b \in \{1, 2, \dots, B+1\}$, is considered. $\phi^{(b)}_i$ and $\psi^{(b)}_i$ are arbitrary coefficients to be determined so that the boundary conditions are satisfied. The normalised strain in block (b) is given by Eq. (47) as

$$\tilde{E}^{(b)}_{f_i}(\xi) = \frac{d\{\tilde{U}^{(b)}(\xi)\}}{d\xi} = -\sum_{\imath=1}^{2N} \left\{C^{(b)}_\imath\right\} \lambda^{(b)}_\imath \left[\phi^{(b)}_\imath \exp(-\lambda^{(b)}_\imath \xi) + \psi^{(b)}_\imath \exp(+\lambda^{(b)}_\imath \xi)\right]. \tag{55}$$

In order to satisfy Eq. (44) in block $b = 1$ as $\xi \to -\infty$, because of Eq. (53), it is necessary that $\psi^{(1)}_\imath \equiv 0$, for all $\imath \in \{1, 2, \dots, 2N\}$. By the same argument for the case $\xi \to \infty$, $\phi^{(B+1)}_\imath \equiv 0$, for all $\imath \in \{1, 2, \dots, 2N\}$. The solution of the present boundary value

problem thus requires the determination of $2NB$ unknown $\phi_\iota^{(b)}$, $\iota \in \{1, 2, \dots, 2N\}$, and $b \in \{1, 2, \dots, B\}$, and $2NB$ unknown $\psi_\iota^{(b)}$, $\iota \in \{1, 2, \dots, 2N\}$, and $b \in \{2, 3, \dots, B+1\}$. To determine these $4NB$ unknowns, $4NB$ equations are needed. The continuity conditions, Eqs. (41), and (42), and the conditions at the fibre break, Eq. (43), yield $2(2N)$ equations each per block boundary. Since there are B block boundaries, there are $4NB$ equations in all, which is adequate to determine the unknowns.

Determination of the eigenvalues and eigenvectors, $\lambda_\iota^{(b)}$ and $\{C_\iota^{(b)}\}$ for the matrices $[A^{(b)}]$, and the solution for $\phi_i^{(b)}$ and $\psi_i^{(b)}$ represent the computationally expensive steps of the present procedure. Substituting the $\phi_i^{(b)}$ and $\psi_i^{(b)}$ obtained above into the Eqs. (54) and (55) yields the normalised auxiliary displacements and strains throughout the composite lamina. The auxiliary fibre loads are then given by Eq. (48).

2.8 Symmetric arrangement of fibre breaks and matrix failure

Suppose at least one fibre break occurs in the plane $x = 0$, and the set of fibre breaks and matrix failure is symmetric about the $x = 0$ or $\xi = 0$ plane. That is, for each fibre break β in fibre F_β, located at the axial position $x = x_\beta$, there is a fibre break β', such that $F_{\beta'} = F_\beta$, but located at the axial position $x_{\beta'} = -x_\beta$. Similarly, for each matrix failure δ in matrix bay M_δ extending over $(x_\delta^{\text{beg}}, x_\delta^{\text{end}})$, there exists a matrix failure δ' such that $M_{\delta'} = M_\delta$ extending over $(-x_\delta^{\text{end}}, -x_\delta^{\text{beg}})$. In this case, symmetry can be exploited to yield computational savings, by representing only half of the composite domain in the computations, say the part $x \geq 0$.

The full model composite is divided into $B+1$ blocks (Sec. 2.3). In the symmetric case, the plane $x = 0$ corresponds to the $(B+1)/2$-th block boundary between blocks $(B+1)/2$, and $(B+1)/2+1$. Blocks $(B+1)/2$, and $(B+1)/2+1$ are mirror images of each other about the plane $x = 0$. This implies

$$-\tilde{U}_{f_i}^{((B+1)/2)}(-\xi) = \tilde{U}_{f_i}^{((B+1)/2+1)}(\xi), \text{ for all } f_i \in \mathscr{L} \cup \mathscr{H}, \text{ and } \xi \in [\xi^{((B+1)/2)}, \xi^{((B+1)/2+1)}]. \tag{56}$$

Together with Eq. (41), for $b = (B+1)/2$, this implies

$$\tilde{U}_{f_i}^{((B+1)/2+1)}(\xi = 0) = 0, \text{ if } i \neq F_\beta, \text{ for all } \beta \in \mathscr{B}^{((B+1)/2)}. \tag{57}$$

In words, symmetry is enforced by demanding zero displacement of intact fibres at the plane $x = 0$. Also, for the case of broken fibres, Eq. (42) implies:

$$\frac{d\tilde{U}_{f_i}^{((B+1)/2+1)}}{d\xi}(\xi = 0) = 0, \text{ if } i = F_\beta, \text{ for any } \beta \in \mathscr{B}^{((B+1)/2)}. \tag{58}$$

In the present symmetric case, Eq. (57) replaces Eq. (41) in block boundary $(B+1)/2$. The unknowns of the boundary value problem are now $\phi_\iota^{(b)}$, and $\psi_\iota^{(b)}$, for $b \in \{(B+1)/2+1, (B+1)/2+2, \dots, B+1\}$. As before, $\phi_\iota^{(B+1)} = 0$, for all $\iota \in \{1, 2, \dots, 2N\}$. It is straightforward to show that the number of unknown $\phi_\iota^{(b)}$ and $\psi_\iota^{(b)}$ is equal to $2NB$. Eqs. (57), and (58), together with Eqs. (41)–(43) applied to block boundaries $((B+1)/2)+1$, $((B+1)/2)+2, \dots, (B)$ suffice to determine these unknowns.

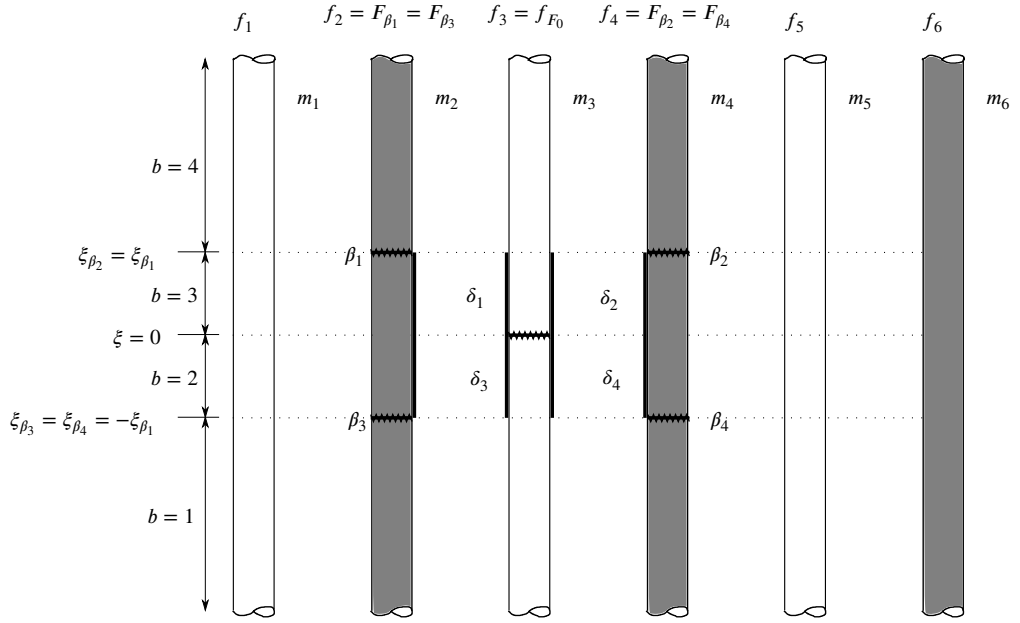

Fig. 3: An illustration of the four symmetric images of fibre break β_1, and matrix failure, δ_1. $\xi = 0$, and fibre f_{F_0} are the symmetry planes of the four-fold symmetry.

2.9 Fracture development

Hitherto, it has been assumed that fibre breaks and/or matrix failure were present prior to far-field load application. A simulation methodology to evolve the state of fracture is now proposed. A typical composite failure simulation begins with one pre-existing fibre break, say $\beta = 0$, at $\xi_\beta = 0$, in fibre f_{F_0}. Presently, the pre-existing break is introduced in an LE fibre, i.e., $f_{F_0} \in \mathscr{L}$. This, together with the deterministic character of the fibre and matrix strengths, implies that fracture develops symmetrically about the $\xi = 0$ plane. That is, provided that $F_{\beta_1} \neq F_0$, and $\xi_{\beta_1} \neq 0$, fibre breaks occur in symmetric sets of four $\{\beta_1, \beta_2, \beta_3, \beta_4\}$ that satisfy

$$F_{\beta_2} = F_{\beta_4} = 2F_0 - F_{\beta_1}, \text{ and } F_{\beta_3} = F_{\beta_1}, \tag{59}$$

and

$$x_{\beta_2} = x_{\beta_1}, \text{ and } x_{\beta_3} = x_{\beta_4} = -x_{\beta_1}. \tag{60}$$

Similarly, matrix failures also occur in sets of four $\{\delta_1, \delta_2, \delta_3, \delta_4\}$, which satisfy:

$$M_{\delta_2} = M_{\delta_4} = 2F_0 - M_{\delta_1} - 1, \text{ and } M_{\delta_3} = M_{\delta_1}, \tag{61}$$

and

$$x^{\text{beg}}_{\delta_2} = x^{\text{beg}}_{\delta_1}, \quad x^{\text{end}}_{\delta_2} = x^{\text{end}}_{\delta_1}, \quad x^{\text{beg}}_{\delta_3} = x^{\text{beg}}_{\delta_4} = -x^{\text{beg}}_{\delta_1}, \text{ and } \quad x^{\text{end}}_{\delta_3} = x^{\text{end}}_{\delta_4} = -x^{\text{end}}_{\delta_1}. \tag{62}$$

A simple example with four symmetric fibre breaks, and four matrix failures is illustrated in Fig. 3. While the symmetry about the transverse $\xi = 0$ plane is treated already in Sec. 2.8, the additional symmetry noted above about fibre f_{F_0} is new.

In the failure simulations, fibre breaks and matrix failure are assumed to be confined within a finite length, $\xi \in [0, \xi_0]$. A numerical value for ξ_0 will be assigned based on the overload profiles near a cluster of fibre breaks in Sec. 3.1 below. The region

$\xi \in [0, \xi_0]$ is discretised by blocks $((B+1)/2+1), ((B+1)/2+2), \ldots, (B)$ (Sec. 2.8). Where there is only the single pre-existing break, $B = 3$, and a single block, $(b = 3)$ covers $\xi \in [0, \xi_0]$ entirely.

Over $\xi \in [0, \xi_0]$, the deterministic strength assigned to both LE and HE fibre elements is denoted P_0; fibre breakage is assumed when

$$p_\infty P_{f_i}^{(b)}(\xi) = \begin{cases} P_0, & \text{if } \xi \in [0, \xi_0], \\ \infty, & \text{if } \xi \in (\xi_0, \infty). \end{cases} \tag{63}$$

Here, $P_{f_i}^{(b)}(\xi)$ is defined in Eq. (49). Similarly, material points in the matrix bays are assigned a deterministic shear strength T_0. Material point failure in matrix bay m_i in block (b) at normalised axial position ξ is assumed to occur when

$$p_\infty T_{m_i}^{(b)}(\xi) = \begin{cases} T_0, & \text{if } \xi \in [0, \xi_0], \\ \infty, & \text{if } \xi \in (\xi_0, \infty). \end{cases} \tag{64}$$

Both P_0 and T_0 have the dimensions of force. By these definitions, fibre breaks, or matrix failures cannot occur in the region $\xi > \xi_0$.

In each of the finite blocks contained in $[0, \xi_0]$, each fibre f_i and matrix bay m_i is discretised by a uniform grid with spacing $\Delta_m^{(b)} = \left(\xi^{(b+1)} - \xi^{(b)}\right)/K$. The fibre-wise stations in this grid are:

$$\xi_k^{(b)} = \xi^{(b)} + k\Delta_m^{(b)}, \text{ for } k \in \{0, 1, \ldots, K\} \text{ and } b \in \{(B+1)/2, (B+1)/2+1, \ldots, B\}. \tag{65}$$

It is presently assumed that $K = 20$. The overloads in the fibres, $P_{f_i}^{(b)}(\xi_k^{(b)})$, and matrix bays, $T_{m_i}^{(b)}(\xi_k^{(b)})$, for $i \in \{1, 2, \ldots, 2N\}$, and $k \in \{0, 1, \ldots, K-1, K\}$ are determined. Let the maximum overload occur in fibre f_{i^*} at $\xi = \xi_{k^*}^{(b^*)}$:

$$P_{f_{i^*}}^{(b^*)}(\xi_{k^*}^{(b^*)}) = \max_{b \in \{(B+1)/2, (B+1)/2+1, \ldots, B\}} \max_{i \in \{1,2,\ldots,2N\}} \max_{k \in \{0,1,\ldots,K\}} P_{f_i}^{(b)}(\xi_k^{(b)}). \tag{66}$$

Similarly, the critical location for matrix failure is that at which $T_{m_i}^{(b)}(\xi_k^{(b)})$ is maximised:

$$T_{m_{i^{**}}}^{(b^{**})}(\xi_{k^{**}}^{(b^{**})}) = \max_{b \in \{(B+1)/2, (B+1)/2+1, \ldots, B\}} \max_{i \in \{1,2,\ldots,2N\}} \max_{k \in \{-K, -(K-1), \ldots, 0, K-1, K\}} T_{m_i}^{(b)}(\xi_k^{(b)}). \tag{67}$$

The far-field load required to break the critical fibres is given by Eqs. (63) and (66) as

$$p_\infty^f = P_0 / P_{f_{i^*}}^{(b^*)}(\xi_{k^*}^{(b^*)}). \tag{68}$$

The far-field load required to initiate matrix failure at the most overloaded matrix bays is given by Eqs. (64) and (67) as

$$p_\infty^{m,0} = T_0 / T_{m_{i^{**}}}^{(b^{**})}(\xi_{k^{**}}^{(b^{**})}). \tag{69}$$

The condition $p_\infty^f \leq p_\infty^{m,0}$ means that matrix failure will not even initiate before a fibre break. In this case, the applied load per fibre is incremented to $p_\infty = p_\infty^f$, and fibre breaks are introduced at the most overloaded fibre location, and its symmetric counterparts, given by Eqs. (59), and (60). If a block boundary does not already exist at the newly introduced fibre breaks, new block boundaries are introduced, and the new blocks are subdivided again following Eq. (65). This completes the present step.

If, however, $p_\infty^f > p_\infty^{m,0}$ matrix failure initiates before fibre failure. To check if the initiated matrix failure will propagate, matrix failures extending over

$$\xi \in \left[\max\left(\xi_{k^{**}}^{(b^{**})} - \delta_m, 0\right), \min\left(\xi_{k^{**}}^{(b^{**})} + \delta_m, \xi_0\right)\right] \tag{70}$$

in matrix bays $m_{i^{**}}$, and its symmetric counterparts, given in Eqs. (61) and (62) are tentatively introduced. Here, δ_m is a fixed increment of normalised matrix failure length. Presently, $\delta_m = 0.005$. The shear stresses are reevaluated for the configuration with the tentative matrix failure. The far-field load per fibre, at which the shear stress at the tips of the tentative matrix failure equals the matrix strength, T_0 is determined using Eq. (64) as:

$$p_\infty^m = \max\left\{\frac{T_0}{T_{m_{i^{**}}}^{(b^*)}\left(\max\left(\xi_{k^{**}}^{(b^{**})} - \delta_m, 0\right)\right)}, \frac{T_0}{T_{m_{i^{**}}}^{(b^*)}\left(\min\left(\xi_{k^{**}}^{(b^{**})} + \delta_m, \xi_0\right)\right)}\right\}. \tag{71}$$

It will be shown in connection with Fig. 7 that

$$p_\infty^{m,0} \leq p_\infty^m, \tag{72}$$

i.e., the far-field stress to propagate the matrix is no smaller than that required to initiate it.

The condition $p_\infty^f \leq p_\infty^m$ means that matrix failure will not propagate before a fibre break. In this case, the applied load per fibre is incremented to $p_\infty = p_\infty^f$, and fibre breaks are introduced at the most overloaded fibre locations (Eqs. (59) and (60)). If a block boundary does not already exist at the newly introduced fibre breaks, new block boundaries are introduced, and the new blocks are subdivided again following Eq. (65). The tentative matrix failure extending over the region specified by Eq. (70), and any block boundaries associated with it are deleted. This represents the end of the present step. However, if $p_\infty^f > p_\infty^m$, the applied load per fibre is incremented to $p_\infty = p_\infty^m$, and the tentative matrix failure, and its symmetric counterparts (Eqs. (61) and (62)) extending over the region specified by Eq. (70) are retained permanently. This operation too completes the present step.

By construction, at every step, either additional fibre breaks, or matrix failures occur. Simulation steps are repeated until the failure of an HE fibre (Zweben 1977). Terminating the simulations at the failure of an HE fibre is justified because, once an HE fibre fails, other fibres in the cross-section of the HE fibre break must be overloaded past their strength P_0. These fibres must fail with no further far-field load increment. A flowchart of the simulation algorithm is given in Fig. 4.

2.10 Fracture energy

Over the course of a fracture simulation, the far-field load per fibre, p_∞ may increase or decrease. The failure event at which p_∞ first attains its maximum value over the simulation is regarded as the point at which crack propagation becomes catastrophic, in a load-controlled experiment. This point may coincide with, or precede the failure of the first HE fibre.

The energy released during fracture of the composite laminate is calculated by summing the incremental energies released by each fibre break and matrix failure event up to the event that just precedes catastrophic crack propagation. The incremental energies, in turn, are obtained using the method of virtual crack closure (Kanninen and Popelar 1985, Sec. 3.3.1). In this method,

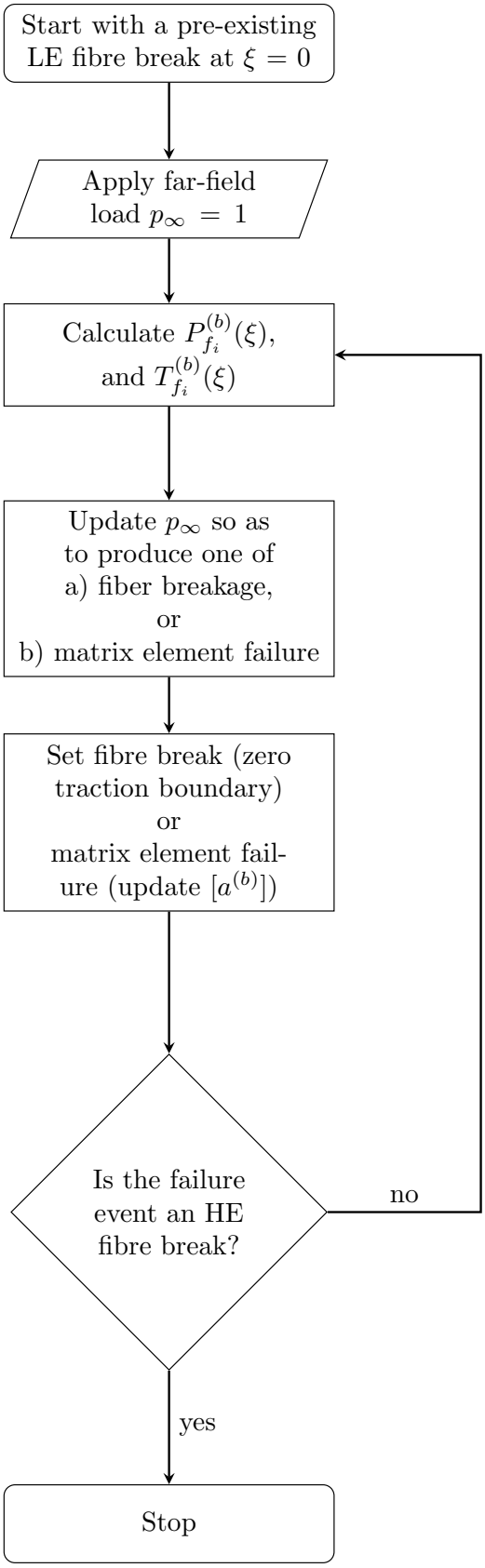

Fig. 4: Flow chart of the fracture simulation of the composite lamina, detailed in Sec. 2.9. The simulation terminates when an HE fibre breaks, following Zweben (1977).

the energy released during a fracture event is equated to the work done by forces applied to the newly created fracture surface, in order to close it. In the general treatment given by Kanninen and Popelar (1985), if a crack of length a and unit depth in a linear elastic body extends self-similarly by Δa, the energy released is:

$$\Delta g = \frac{1}{2}\int_{a'=0}^{\Delta a} \boldsymbol{u}(a')\big|_{\text{after}} \cdot \boldsymbol{t}(a')\big|_{\text{before}}\, da' \tag{73}$$

Here, $\boldsymbol{u}(a')|_{\text{after}}$ is the vector crack opening displacement at a distance of a' from the extended crack tip, along the crack line, after crack extension, and $\boldsymbol{t}(a')|_{\text{before}}$ is the traction vector at a' before crack extension. The traction after crack extension is assumed to be zero. Both $\boldsymbol{u}(a')|_{\text{after}}$ and $\boldsymbol{t}(a')|_{\text{before}}$ may have components both parallel and perpendicular to the crack faces.

Eq. (73) can be used to obtain the energy released by fibre breaks, and matrix failures. Consider a fibre break in fibre f_i located at the b-th block boundary i.e., at normalised axial position $\xi^{(b)}$. In this case, both $\boldsymbol{u}_{\text{open}}(a')$ and $\boldsymbol{t}(a')$ are directed along the axial x-direction, by the present shear-lag assumptions. Also, $\boldsymbol{u}_{\text{open}}(a')$ and $\boldsymbol{t}(a')$ are assumed uniform over the fibre cross-sectional area, A. Therefore, the energy released due to fibre break β, as given by Eq. (73) becomes

$$\begin{aligned}\Delta g_{f_{F_\beta}} &= \left[u^{(b+1)}_{f_{F_\beta}}(x_b) - u^{(b)}_{f_{F_\beta}}(x_b)\right]\Big|_{\text{after}} p_{f_{F_\beta}}\Big|_{\text{before}},\\ &= \left[U^{(b+1)}_{f_{F_\beta}}(\xi^{(b)}) - U^{(b)}_{f_{F_\beta}}(\xi^{(b)})\right]\frac{dU^{(b)}_{f_{F_\beta}}}{d\xi}\frac{p_\infty^2}{\sqrt{k_0 S}},\end{aligned} \tag{74}$$

for all $f_i \in \mathscr{L} \cup \mathscr{H}$. It is reemphasised that the factor $\left[U^{(b+1)}_{f_{F_\beta}}(\xi^{(b)}) - U^{(b)}_{f_{F_\beta}}(\xi^{(b)})\right]$ refer to the displacements after the formation of break β and the factor $\frac{dU^{(b)}_{f_{F_\beta}}}{d\xi}$ to the displacements before the formation of this break. The normalised energy release due to a break is defined as

$$\Delta G_{f_{F_\beta}} = \frac{\Delta g_{f_{F_\beta}}}{p_\infty^2/\sqrt{k_0 S}}. \tag{75}$$

Next, consider a matrix failure in matrix bay, m_i, extending from $x = x^{(b)}$ to $x = x^{(b+1)}$. Let the shear strain in the matrix bay before and after failure be $\gamma_{m_i}\Big|_{\text{before}} = (u_{f_{[i+1]}} - u_{f_i})/w\Big|_{\text{before}}$, and $\gamma_{m_i}\Big|_{\text{after}} = (u_{f_{[i+1]}} - u_{f_i})/w\Big|_{\text{after}}$, respectively. Then, according to Eq. (73), the energy released during matrix failure is given by

$$\begin{aligned}\Delta g_{m_i} &= \int_{x'=x^{(b)}}^{x^{(b+1)}} G\,\frac{u_{f_{[i+1]}} - u_{f_i}}{w}\Big|_{\text{before}}\left\{\frac{u_{f_{[i+1]}} - u_{f_i}}{w}\Big|_{\text{after}} - \frac{u_{f_{[i+1]}} - u_{f_i}}{w}\Big|_{\text{before}}\right\} w d\, dx',\\ &= \begin{cases}\frac{p_\infty^2}{\sqrt{k_0 S}}\int_{\xi'=\xi^{(b)}}^{\xi^{(b+1)}} \frac{U^{(b)}_{f_{[i+1]}}}{\sqrt{\eta_{\text{HE}}}} - \frac{U^{(b)}_{f_i}}{\sqrt{\eta_{\text{LE}}}}\Big|_{\text{before}}\left\{\frac{U^{(b)}_{f_{[i+1]}}}{\sqrt{\eta_{\text{HE}}}} - \frac{U^{(b)}_{f_i}}{\sqrt{\eta_{\text{LE}}}}\Big|_{\text{after}} - \frac{U^{(b)}_{f_{[i+1]}}}{\sqrt{\eta_{\text{LE}}}} - \frac{U^{(b)}_{f_i}}{\sqrt{\eta_{\text{HE}}}}\Big|_{\text{before}}\right\} d\xi', & \text{if } f_i \in \mathscr{L}\\ \frac{p_\infty^2}{\sqrt{k_0 S}}\int_{\xi'=\xi^{(b)}}^{\xi^{(b+1)}} \frac{U^{(b)}_{f_{[i+1]}}}{\sqrt{\eta_{\text{LE}}}} - \frac{U^{(b)}_{f_i}}{\sqrt{\eta_{\text{HE}}}}\Big|_{\text{before}}\left\{\frac{U^{(b)}_{f_{[i+1]}}}{\sqrt{\eta_{\text{LE}}}} - \frac{U^{(b)}_{f_i}}{\sqrt{\eta_{\text{HE}}}}\Big|_{\text{after}} - \frac{U^{(b)}_{f_{[i+1]}}}{\sqrt{\eta_{\text{LE}}}} - \frac{U^{(b)}_{f_i}}{\sqrt{\eta_{\text{HE}}}}\Big|_{\text{before}}\right\} d\xi', & \text{if } f_i \in \mathscr{H}.\end{cases}\end{aligned} \tag{76}$$

The normalised energy released in the course of failure in a single matrix bay is defined as

$$\Delta G_{m_i} = \frac{\Delta g_{m_i}}{p_\infty^2/\sqrt{k_0 S}}. \tag{77}$$

The total (normalised) energy released is simply the sum over (normalised) energy releases in the course of each fibre breakage and matrix failure:

$$\Delta e = \sum_{\beta} \Delta g_{f_{F_\beta}} + \sum_{\delta} \Delta g_{m_{M_\delta}}, \text{ and}$$
$$\Delta E = \sum_{\beta} \Delta G_{f_{F_\beta}} + \sum_{\delta} \Delta G_{m_{M_\delta}}. \tag{78}$$

3 Results

3.1 Overloads near a single break

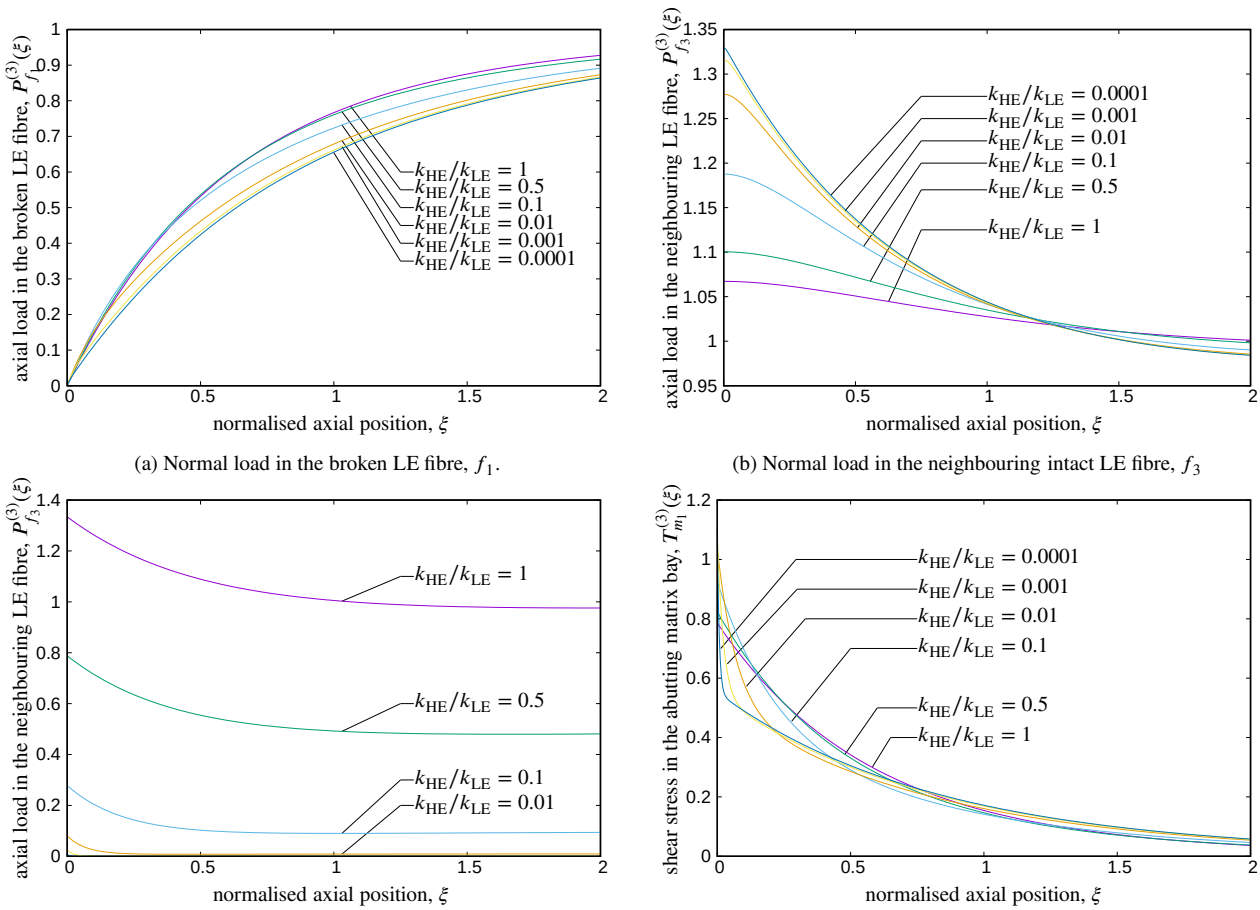

(a) Normal load in the broken LE fibre, f_1.

(b) Normal load in the neighbouring intact LE fibre, f_3

(c) Normal load in the neighbouring intact HE fibre, f_2.

(d) Shear stress in the matrix bay m_1 abutting the broken fibre

Fig. 5: Normalised axial load and normalised shear stresses near a single fibre break in f_1 at $\xi = 0$. (a) Axial load in the broken LE fibre, f_1; (b) axial load in the neighbouring intact LE fibre, f_3; (c) axial load in the neighbouring intact HE fibre, f_2; and (d) Shear stress in the matrix bay m_1 abutting the broken fibre.

Consider an infinitely long model composite comprised of $N = 20$ LE, and $N = 20$ HE fibres. The fibre f_1 is broken at $\xi = 0$. The normalised normal load in the fibres, $P^{(b)}_{f_i}(\xi)$ and the normalised shear stresses in matrix bays $T^{(b)}_{m_i}(\xi)$ abutting the

broken LE fibre, f_1, are evaluated assuming $p_\infty = 1$. It is henceforth assumed that

$$k_0 = k_{\mathrm{LE}}, \tag{79}$$

so that the total load applied at the far-field becomes $N(1 + k_{\mathrm{HE}}/k_{\mathrm{LE}})$, according to Eq. (11). The model composite is discretised into four blocks; these blocks extend over $(-\infty, -2)$, $(-2, 0)$, $(0, 2)$, and $(2, \infty)$. The results in Sec. 3.1, and 3.2 are shown for the block ($b = 3$).

The axial load variation with axial distance from the break in the broken fibre, $P^{(3)}_{f_1}(\xi)$, is shown in Fig. 5a. As in the classical Hedgepeth (1961) and Zweben (1977) models, the load build up with ξ has an exponential form. The distance ξ_0 required to regain $1 - 1/e$ of the far-field load may be regarded as a characteristic distance. Clearly, ξ_0 increases with decreasing $k_{\mathrm{HE}}/k_{\mathrm{LE}}$, i.e., load in the broken fibre is regained more rapidly in composite laminae with larger $k_{\mathrm{HE}}/k_{\mathrm{LE}}$: $\xi_0 = 0.68$ at $k_{\mathrm{HE}}/k_{\mathrm{LE}} = 1$, but increases to $\xi_0 = 0.94$ for $k_{\mathrm{HE}}/k_{\mathrm{LE}} = 0.001$.

Figs. 5b and 5c show the build up of normal loads in the LE and HE fibres abutting the broken fibre, respectively. The LE normal loads at the break plane, $\xi = 0$ decreases with increasing $k_{\mathrm{HE}}/k_{\mathrm{LE}}$. The HE normal loads has the opposite trend. Away from the plane $\xi = 0$, the LE and HE fibre loads approach p_∞, and $(k_{\mathrm{HE}}/k_{\mathrm{LE}})p_\infty$, respectively. This convergence is nearly complete by about $\xi = 1$ for all $k_{\mathrm{HE}}/k_{\mathrm{LE}}$.

The normalised shear stresses in the matrix bay m_1 abutting fibre f_1 are shown in Fig. 5d. The shear stresses at the break plane become greater near the fibre with decreasing $k_{\mathrm{HE}}/k_{\mathrm{LE}}$. For $\xi \geq 1$, the decay of the shear stresses with ξ becomes similar for all $k_{\mathrm{HE}}/k_{\mathrm{LE}}$. The magnitude of the shear stresses at $\xi = 1$ also drops to less than $1/e$ of the peak values achieved at $\xi = 0$ for all $k_{\mathrm{HE}}/k_{\mathrm{LE}}$.

In their 'chain of bundles' model, Gücer and Gurland (1962) and Rosen (1964) proposed that the composite may be subdivided in the fibre direction into mechanically non-interacting layers of length $2\delta_0$, as shown in Fig. 1. Also, in Sec. 2.9, it was proposed to account for fibre and matrix failure only within the normalised length $\xi \in [-\xi_0, \xi_0]$. The foregoing results show that for any $k_{\mathrm{HE}}/k_{\mathrm{LE}}$, if fibre breaks are more than $\Delta\xi = 2$ apart, they may approximately be regarded as mechanically non-interacting. These considerations imply that a suitable non-dimensional length of the simulation cell is

$$\xi_0 = 1, \tag{80}$$

which, together with Eq. (34) implies that

$$\delta_0 = \xi_0 \cdot \sqrt{\frac{k_0}{S}} = \sqrt{\frac{k_0}{S}}, \tag{81}$$

in Fig. 1.

3.2 Overloads near a broken fibre with matrix failure in the adjacent bays

The loads in the vicinity of a fibre break at $\xi = 0$ in fibre f_1, with matrix failures in its abutting matrix bays m_1 and m_{40} in an $N = 20$ lamina (lamina comprised of an alternating arrangement of 20 LE and 20 HE fibres) is shown in Fig. 6. The configuration

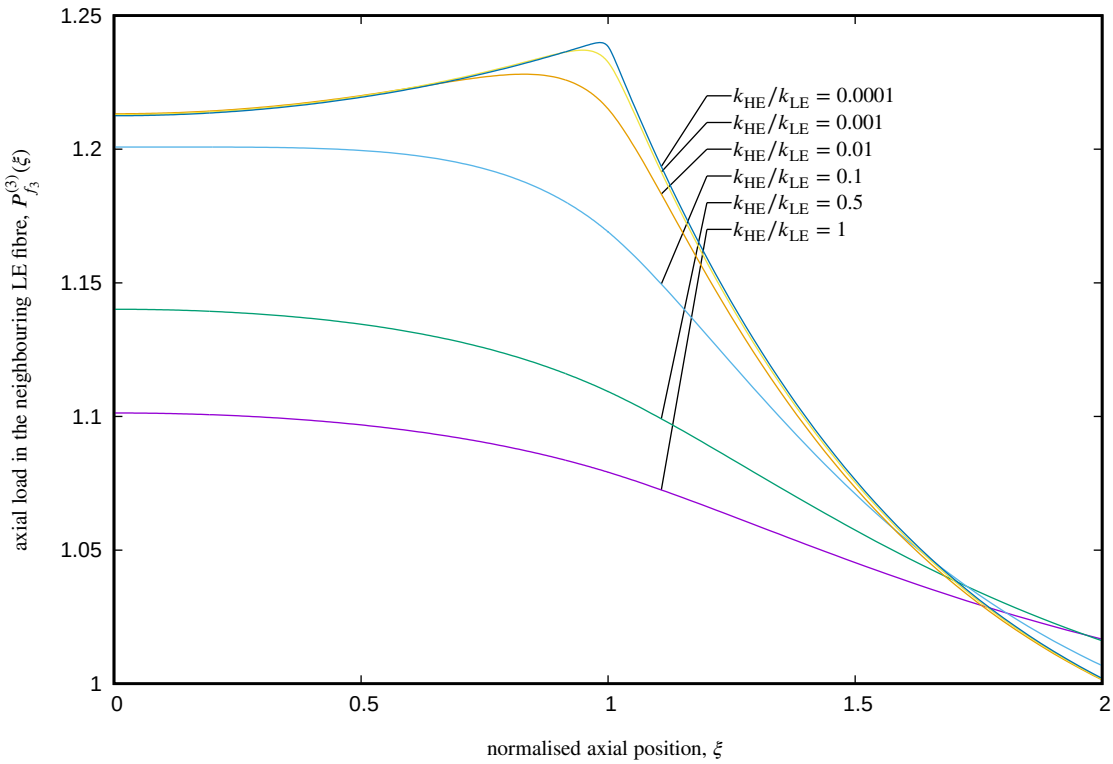

(a) Axial load in the neighbouring intact LE fibre, f_3

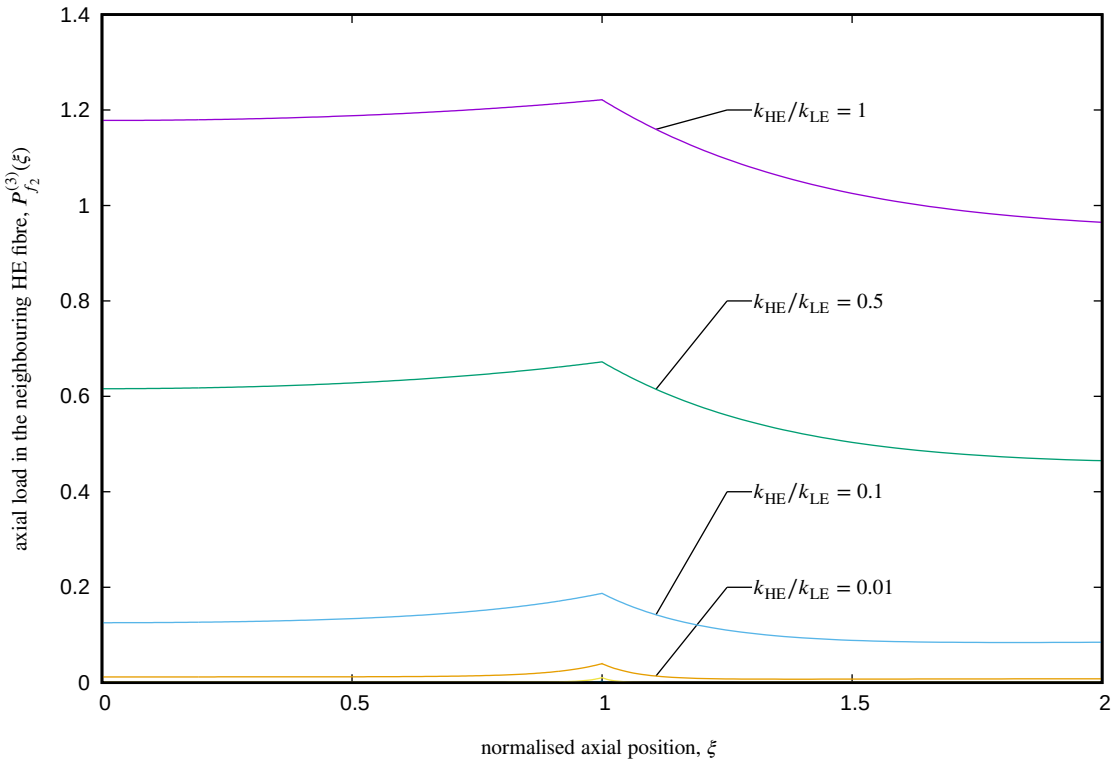

(b) Axial load in the neighbouring intact intact HE fibre, f_2.

Fig. 6: Normalised axial load in the vicinity of a fibre break at $\xi = 0$ in fibre f_1. (a) Axial load in the neighbouring intact LE fibre, f_3; (b) Axial load in the neighbouring intact HE fibre, f_2.

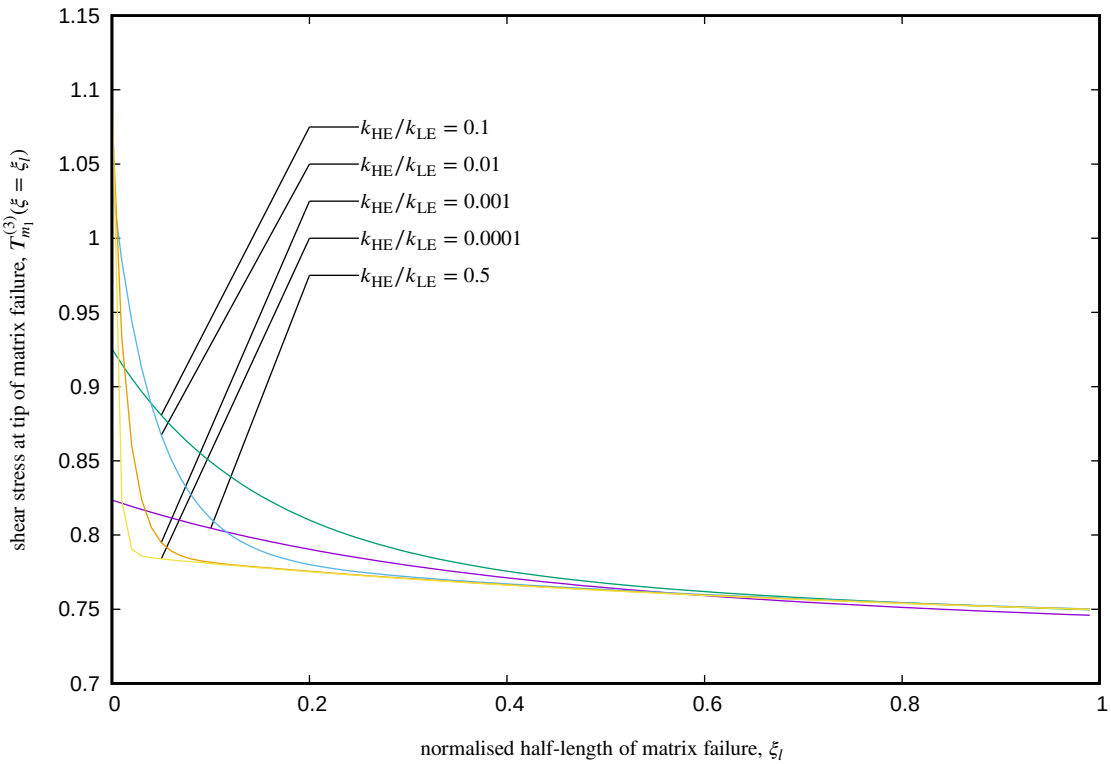

Fig. 7: Variation of the normalised shear stress $T^{(3)}_{m_1}$ at the tip of matrix failure $\xi = \xi_l$ with the length of the failed matrix. The shear stress asymptotes to a constant non-zero value as $\xi_l \to \infty$, which is independent of k_{HE}/k_{LE}.

of fibre breaks and matrix tears is shown in Fig. 2a. The matrix failures extend over $x \in (-\delta_0, \delta_0)$, or $\xi \in (-1, 1)$, where δ_0 is given by Eq. (81). The applied load at $\xi = \pm\infty$ is $p_\infty = 1$.

The stress in the broken fibre f_1 remains zero over $\xi \in (-1, 1)$. Because of the matrix failure, no load transfer to the broken fibre occurs over this range. The matrix failure also qualitatively affects the variation of the normal loads in the neighbouring fibres. Most notably, as seen in Fig. 6a, the load in the neighbouring LE fibre f_3 maximises for small $k_{HE}/k_{LE} \leq 0.01$ not at $\xi = 0$, but at $\xi = 1$, where the matrix failure ends. The matrix failure reduces the loads in the plane $\xi = 0$ for these cases, as seen by comparing with Fig. 5b. For larger k_{HE}/k_{LE}, however, the axial load in the neighbouring LE fibre maximises at $\xi = 0$. Furthermore, the maximum load at $\xi = 0$ for larger k_{HE}/k_{LE} exceeds that obtained without the matrix failure. This is again seen by comparing with Fig. 5b.

Fig. 6b shows the load variations in the HE fibre f_2, adjacent to the broken fibre. The maximum load occurs not in the plane of the fibre break, but at the edge of the matrix failure, for all k_{HE}/k_{LE}. Matrix failure reduces the loads in the adjacent HE fibre at $\xi = 0$. This is seen by comparing with Fig. 5c.

The shear stress at the tip of a failed matrix determines its propagation, according to Eq. (71). Consider a fibre break located at $\xi = 0$ in fibre f_1. Let the matrix bays m_1 and m_{40} abutting the broken fibre fail over the normalised length $-\xi_l \leq \xi \leq \xi_l$, as shown in Fig. 2a. The variation of the normalised shear stress at the tip of the matrix failure, as a function of half-length ξ_l is

shown in Fig. 7. For all $k_{\mathrm{HE}}/k_{\mathrm{LE}}$, the normalised shear stress at the tip, $T^{(3)}_{m_1}(\xi = \xi_l)$, decreases monotonically with increasing ξ_l. For large ξ_l, $T^{(3)}_{m_1}(\xi = \xi_l) \approx 0.75$ asymptotically, for all $k_{\mathrm{HE}}/k_{\mathrm{LE}}$. These observations justify Eq. (72) stated previously.

3.3 Failure mechanisms

Attention is presently restricted to the case of a composite reinforced by two types of fibres, with stiffness k_{LE} and k_{HE}, but with equal deterministic tensile strength, P_0. It is assumed that the matrix shear strength,

$$T_0 = 1 \text{ force unit.} \tag{82}$$

This assumption involves no loss of generality, because, hybrid composite strength scales linearly with T_0. According to Eq. (31), this also applies to the fracture strain. Eq. (74) shows that the fracture energy must scale as T_0^2.

Notwithstanding its apparent simplicity, the present shear-lag model displays a variety of failure mechanisms. These mechanisms are systematically characterised presently as a function of two parameters: (i) the ratio of fibre stiffnesses, $k_{\mathrm{HE}}/k_{\mathrm{LE}}$, and (ii) the fibre strength, P_0/T_0. To this end, computer failure simulations have been performed for a number of $(k_{\mathrm{HE}}/k_{\mathrm{LE}}, P_0/T_0)$ pairs, following the approach detailed in Sec. 2.9. In these simulations, fibre and matrix failure events are restricted to only one representative slice of the composite lamina of normalised length $2\xi_0$, ranging from $-\xi_0 \leq \xi \leq \xi_0$; for ξ_0 specified in Eq. (80). A pre-existing fibre break is assumed in fibre $f_{F_0} = f_1$ at position $\xi = 0$. Infinite blocks $b = 1$ and $b = B + 1$ are assumed to extend over $\xi \in (-\infty, -\xi_0)$, and $\xi \in (\xi_0, \infty)$.

For the case $k_{\mathrm{HE}}/k_{\mathrm{LE}} = 1$, the terminology of LE and HE fibres is only nominal. When sufficiently loaded, the two neighbouring fibres of the initially broken fibre fail in the plane $\xi = 0$. This configuration of three breaks is catastrophic, i.e., no further load increase is needed to propagate the cluster of three breaks. For fixed P_0/T_0, as $k_{\mathrm{HE}}/k_{\mathrm{LE}}$ decreases, the fraction of the applied load carried by the LE fibres increases, and that carried by the HE fibres decreases. Fig. 8 shows three qualitatively different developments leading up to the catastrophic crack corresponding to $k_{\mathrm{HE}}/k_{\mathrm{LE}} \in \{0.3, 0.05, 0.01\}$. In these three cases, $P_0/T_0 = 0.3$.

The first column shows the variation of the applied load with each failure event in the composite. Red diamonds denote LE fibre breaks, and the black circle denotes the first HE fibre break, at which the failure simulation is terminated. Blue inverted triangles denote matrix failure events. The second column shows the partially fractured state of the composite when the simulation is terminated, which occurs with the failure of an HE fibre.

The applied load evolution and the sequence of breaks formed up to the point of failure of a HE fibre, for a composite with $k_{\mathrm{HE}}/k_{\mathrm{LE}} = 0.3$, are shown in Figs. 8a and 8b. A catastrophic cluster of breaks forms upon the breakage of the neighbours of the initial break. At this point, the applied load is at its maximum value. But the first HE fibre breaks only after all the LE fibres are broken.

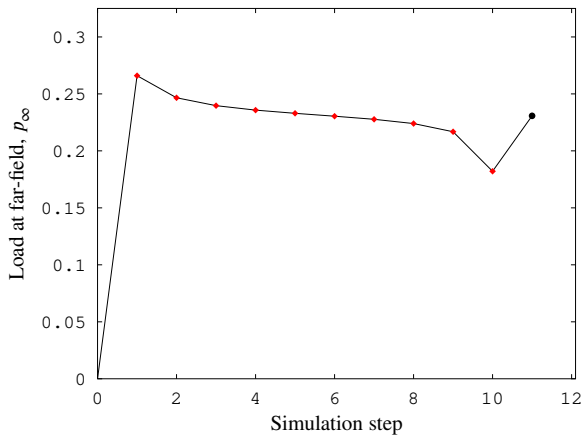

(a) $k_{HE}/k_{LE} = 0.3$; $P_0/T_0 = 0.3$

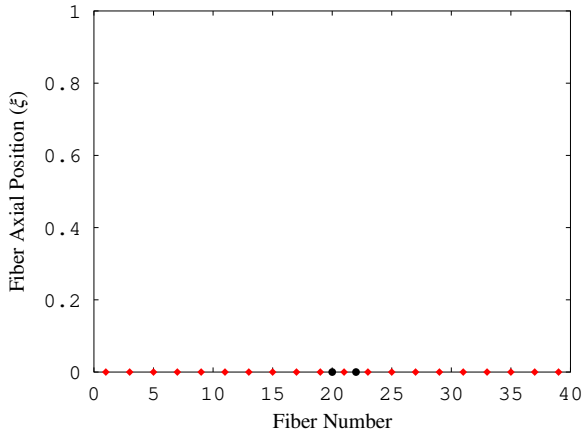

(b) $k_{HE}/k_{LE} = 0.3$; $P_0/T_0 = 0.3$

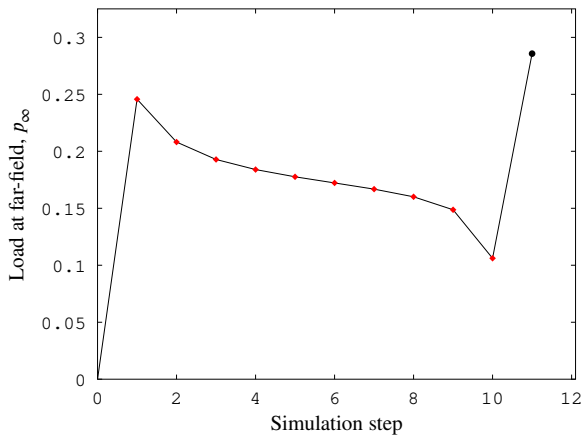

(c) $k_{HE}/k_{LE} = 0.05$; $P_0/T_0 = 0.3$

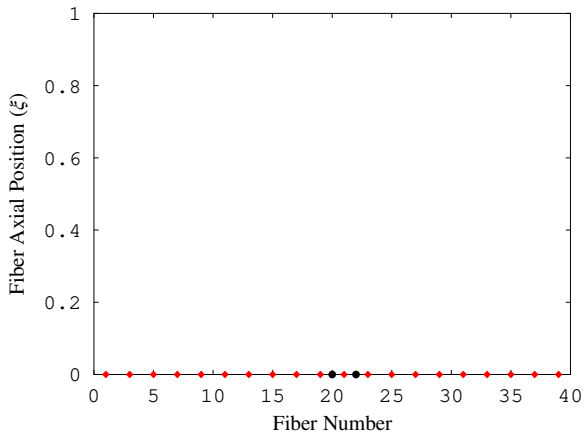

(d) $k_{HE}/k_{LE} = 0.05$; $P_0/T_0 = 0.3$

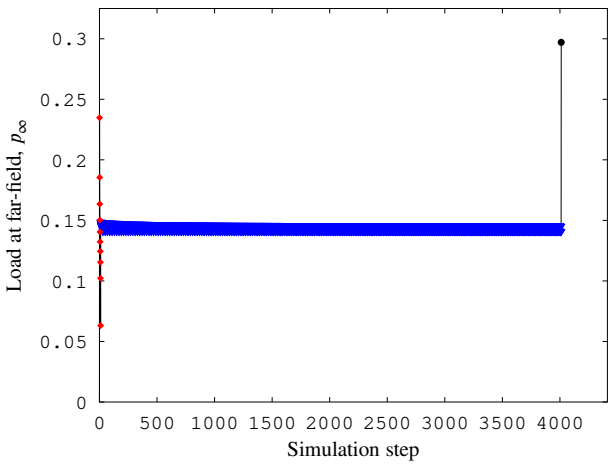

(e) $k_{HE}/k_{LE} = 0.01$; $P_0/T_0 = 0.3$

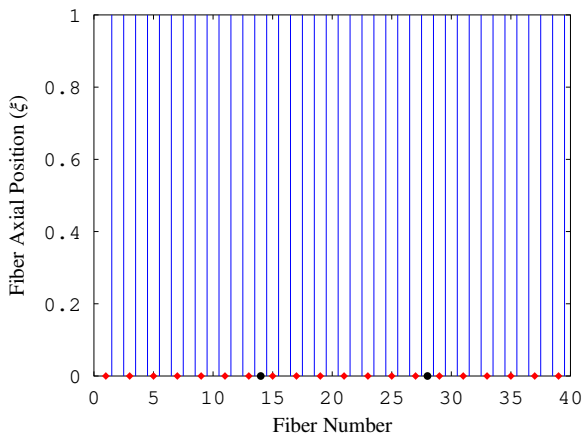

(f) $k_{HE}/k_{LE} = 0.01$; $P_0/T_0 = 0.3$

Fig. 8: (a, c, e) Evolution of far-field load up to the point of breakage of a HE fibre. (b, d, f) Partially fractured state immediately after the HE fibre break. (a, b) correspond to point A, (c, d) correspond to point B, and (e, f) correspond to point C in Fig. 10. ◆ indicates stiff fibre breaks, ● indicate HE fibre breaks, ▽ and — indicates matrix failures.

Let p_{LE}, and p_{HE} denote the far-field load per fibre when the first LE and HE fibres break, respectively. In the present case, $p_{\mathrm{LE}} = 0.266 > p_{\mathrm{HE}} = 0.230$. When all the LE fibres are broken, the HE fibres are in a state of equal load sharing, i.e., the load on all the HE fibres, $P^{(b)}_{f_i}(\xi = 0) = 1 + k_{\mathrm{HE}}/k_{\mathrm{LE}} = 1 + 0.3 = 1.3$, for $f_i \in \mathscr{H}$. The failure of one of these HE fibres therefore, occurs according to Eq. (63), when $p_\infty = P_0/T_0/1.3 = 0.23$. This deduced value is seen to agree with the p_∞ at which HE failure occurs, according to Fig. 8a.

For lower $k_{\mathrm{HE}}/k_{\mathrm{LE}} = 0.05$, keeping $P_0/T_0 = 0.3$ fixed, the load evolution and fracture state immediately after the failure of the first HE fibre are shown in Figs. 8c and 8d. Here, the a large far-field load is required to break the neighbours of the initially-broken LE fibre. Subsequent LE fibre breaks form at progressively decreasing far-field load. However, after all the LE fibres are broken, an increase in far-field load is necessary in order to break an HE fibre. This is because the stress concentrations in all the HE fibres become equal after the failure of all LE fibres, with a value of $P^{(b)}_{f_i}(\xi = 0) = 1 + k_{\mathrm{HE}}/k_{\mathrm{LE}} = 1.05$, for $f_i \in \mathscr{H}$. The HE fibre itself therefore fails according to Eq. (63), when $p_\infty = 0.286$. After the failure of this HE fibre, the far-field load will decrease monotonically (not shown). This case is qualitatively different from that of $k_{\mathrm{HE}}/k_{\mathrm{LE}} = 0.3$ in that the catastrophic crack propagation initiates only after the failure of an HE fibre, i.e., $p_{\mathrm{LE}} = 0.246 < p_{\mathrm{HE}} = 0.286$.

At still lower $k_{\mathrm{HE}}/k_{\mathrm{LE}} = 0.01$, keeping $P_0/T_0 = 0.3$ fixed, matrix failure occurs after the failure of all the LE fibres, and before the failure of the first HE fibre. This is shown in Figs. 8e and 8f. The matrix failure propagates up to the maximum permitted length of $\xi_0 = \pm 1$ on each side of the failure plane, $\xi = 0$ at all the matrix bays m_i in the model. As with $k_{\mathrm{HE}}/k_{\mathrm{LE}} = 0.05$, and unlike $k_{\mathrm{HE}}/k_{\mathrm{LE}} = 0.3$, the peak load is reached only upon failure of an HE fibre, at $p_{\mathrm{LE}} = 0.235 < p_{\mathrm{flexible}} = 0.297$.

Matrix failure becomes important with increasing P_0/T_0. This is illustrated by fixing $P_0/T_0 = 1.6$, in Fig. 9, for three values of $k_{\mathrm{HE}}/k_{\mathrm{LE}} \in \{0.7, 0.3, 0.01\}$. Figs. 9a and 9b show the development of fracture with the far-field applied load, p_∞, and the partially fractured state in the model composite at the point of failure of the first HE fibre. Even for $k_{\mathrm{HE}}/k_{\mathrm{LE}}$ as high as 0.7, some matrix failure, interspersed with LE fibre failures occurs. The first HE fibre fails after the breakage of four LE fibres.

Keeping $P_0/T_0 = 1.6$ fixed, if now $k_{\mathrm{HE}}/k_{\mathrm{LE}}$ were lowered, more LE fibre failures and more extensive matrix failure precedes the failure of the first HE fibre. In Figs. 9c and 9d, corresponding to $k_{\mathrm{HE}}/k_{\mathrm{LE}} = 0.3$ and in Figs. 9e and 9f, corresponding to $k_{\mathrm{HE}}/k_{\mathrm{LE}} = 0.01$, all the LE fibres and all the matrix bays fail before the failure of an HE fibre. The distinctive feature of the failure of the $k_{\mathrm{HE}}/k_{\mathrm{LE}} = 0.01$ model composite, as shown in Fig. 9f, is that the failing LE fibres lie outside the plane $\xi = 0$.

3.4 The $(P_0/T_0, k_{\mathrm{HE}}/k_{\mathrm{LE}})$ parameter space

Fracture development over the $(P_0/T_0, k_{\mathrm{HE}}/k_{\mathrm{LE}})$ parameter space is systematically studied for

$$P_0/T_0 \in \{0.01, 0.05, 0.10, 0.12, \ldots, 0.20, 0.3, 0.4, \ldots, 2.0\}, \text{ and} \tag{83}$$

$$k_{\mathrm{HE}}/k_{\mathrm{LE}} \in \{0.0001, 0.0005, 0.001, 0.005, 0.01, 0.05, 0.1, 0.2, \ldots, 1.0\}. \tag{84}$$

Fracture for each $(P_0/T_0, k_{\mathrm{HE}}/k_{\mathrm{LE}})$ is studied in an $N = 20$ hybrid composite comprised of 20 LE and 20 HE fibres.

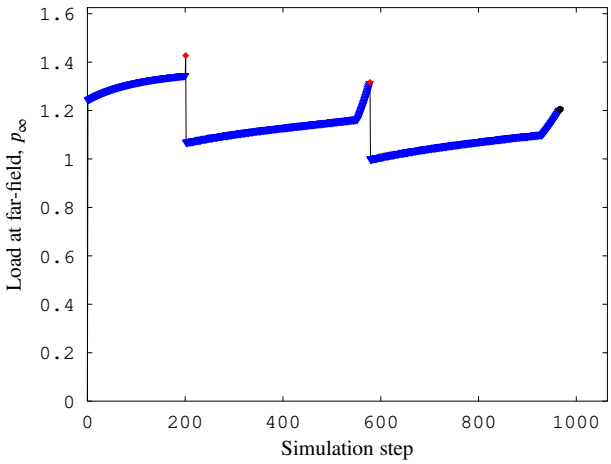

(a) $k_{HE}/k_{LE} = 0.7$; $P_0/T_0 = 1.6$

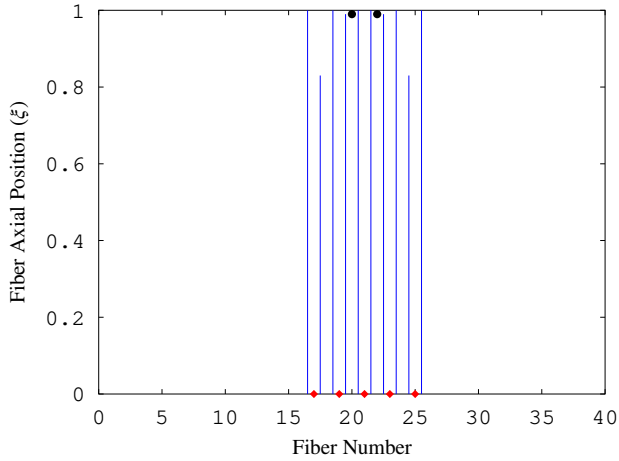

(b) $k_{HE}/k_{LE} = 0.7$; $P_0/T_0 = 1.6$

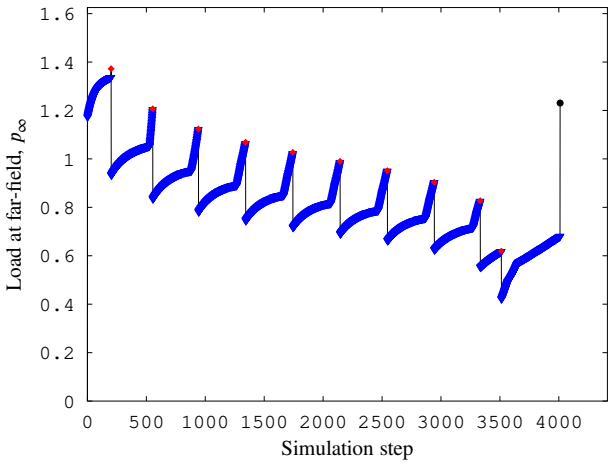

(c) $k_{HE}/k_{LE} = 0.3$; $P_0/T_0 = 1.6$

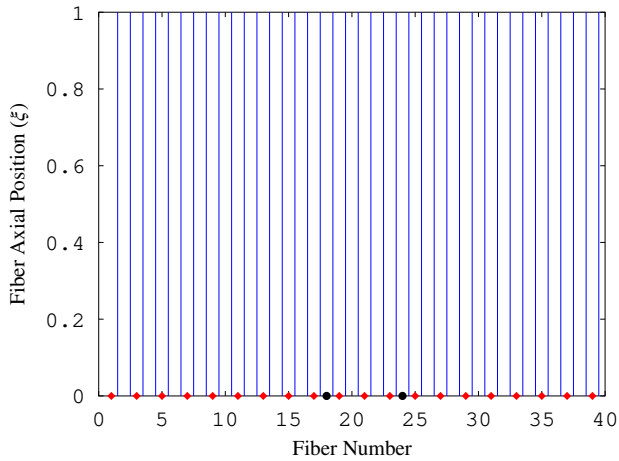

(d) $k_{HE}/k_{LE} = 0.3$; $P_0/T_0 = 1.6$

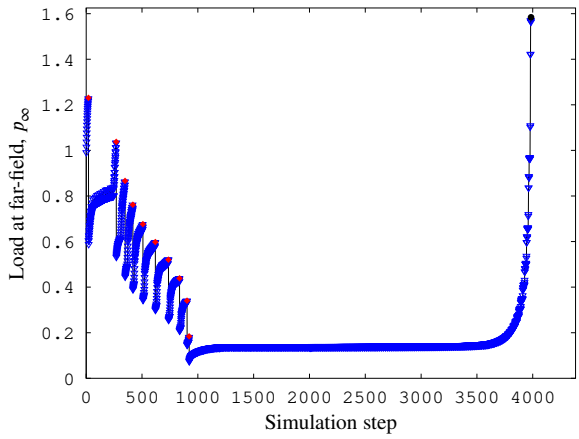

(e) $k_{HE}/k_{LE} = 0.01$; $P_0/T_0 = 1.6$

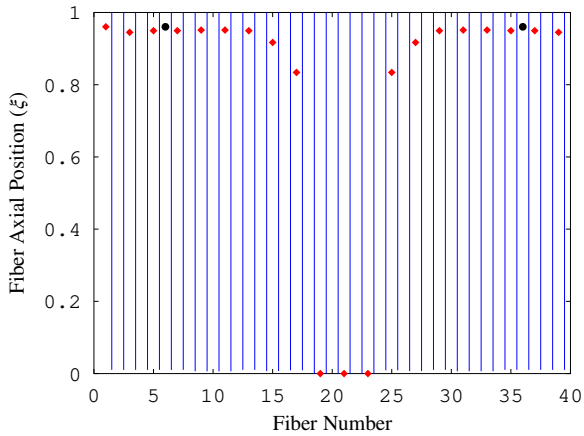

(f) $k_{HE}/k_{LE} = 0.01$; $P_0/T_0 = 1.6$

Fig. 9: (a, c, e) Evolution of far-field load up to the point of breakage of a HE fibre. (b, d, f) Partially fractured state immediately after the HE fibre break. (a, b) correspond to point D, (c, d) correspond to point E, and (e, f) correspond to point F in Fig. 10. ◆ indicates LE fibre breaks, ● indicates HE fibre breaks, and ▽ and — indicate matrix failures.

Table 1: Qualitative fracture modes associated with each of the zones $Z_1, Z_2, \ldots, Z_6$ in Fig. 10.

Zone	LE fibre failure is catastrophic	Matrix failure before HE fibre break	Matrix failure before LE fibre break
Z_1	Yes	No	No
Z_2	No	No	No
Z_3	Yes	Yes	No
Z_4	No	Yes	No
Z_5	Yes	Yes	Yes
Z_6	No	Yes	Yes

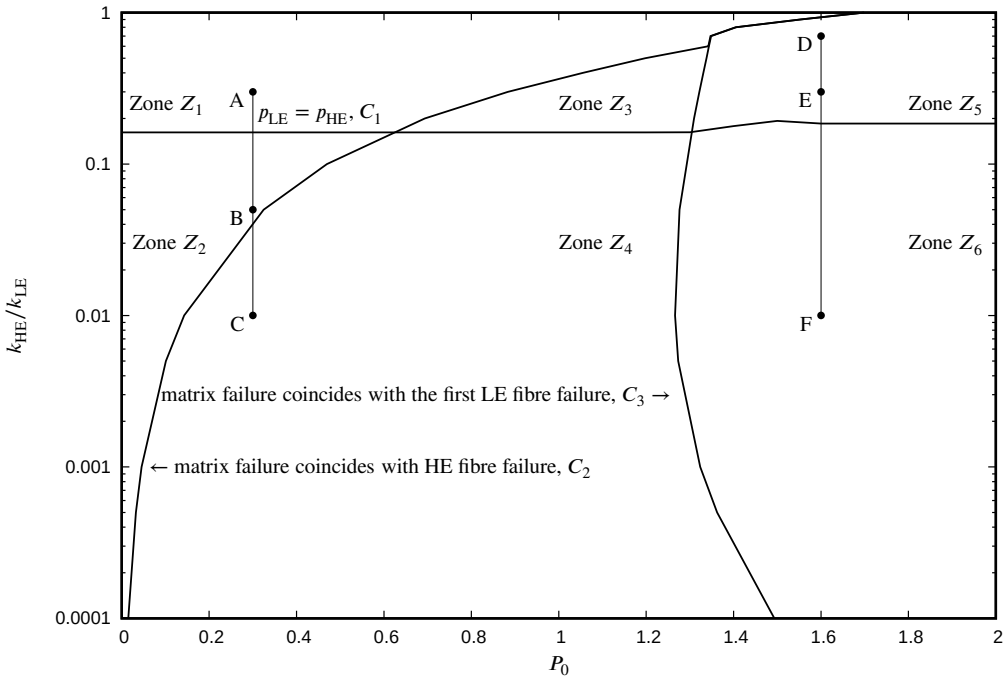

Fig. 10: Division of the $(P_0/T_0, k_{HE}/k_{LE})$ parameter space into six zones, corresponding to qualitatively different fracture modes, as summarised in Table 1. The dividing curves, C_1, C_2, and C_3 are computed as described in the text. Points A, B, and C correspond to the parameter pairs discussed in Fig. 8, and points D, E, and F to those discussed in Fig. 9.

First, the $(P_0/T_0, k_{HE}/k_{LE})$ parameter space can be divided into two parts, corresponding to $p_{LE} < p_{HE}$, and $p_{LE} > p_{HE}$. The transition line, which corresponds to $p_{LE} = p_{HE}$ is computed by evaluating p_{LE}, and p_{HE}, over each of the grid points in Eq. (83). For each P_0/T_0, a pair of neighbouring k_{HE}/k_{LE} grid points which correspond to $p_{LE} < p_{HE}$ and $p_{LE} > p_{HE}$ is identified. The interval between this pair is bisected repeatedly to determine the k_{HE}/k_{LE} for which $p_{LE} = p_{HE}$ to an accuracy of 10^{-4}. The curve so obtained is shown in Fig. 10 marked '$p_{LE} = p_{HE}$, C_1'.

Similarly, matrix failure before HE fibre failure occurs only for certain parameter combinations, $(P_0/T_0, k_{HE}/k_{LE})$. A systematic division of the parameter space into a region of no matrix failure before HE fibre failure, and a region wherein some or extensive matrix failure occurs during the simulation has been carried out, again using the procedure outlined in the previous

paragraph. This separating curve is also shown in Fig. 10, marked 'matrix failure coincides with HE fibre failure'. In the areas to the right of this curve, matrix failure precedes HE fibre failure. In the areas to the left of this curve, HE fibre failure occurs first. Since the simulations terminate at the point of HE fibre failure, no matrix failure is observed in to the left of the curve labelled matrix failure coincides with HE fibre failure'.

Finally, matrix failure may initiate either before the failure of an LE fibre (excluding the pre-existing LE break), or initiate after the failure of an LE fibre. A curve that separates these two regions is again computed and is shown in Fig. 10 labelled 'matrix failure coincides with first LE fibre failure'. In the areas of the parameter space to the right of this curve, matrix failure precedes the first LE fibre failure. To the left of this curve, matrix failure follows the first LE failure. The curves 'matrix failure coincides with HE fibre failure' and 'matrix failure coincides with the first LE fibre failure' meet at $P_0/T_0 = 1.344$, $k_{\mathrm{HE}}/k_{\mathrm{LE}} = 0.6$. At this point, matrix failure, first LE fibre failure, and HE fibre failure occur together.

The three curves, described above, which separate regions of the parameter space that correspond to qualitatively different routes of fracture development are henceforth termed C_1 ($p_{\mathrm{LE}} = p_{\mathrm{HE}}$), C_2 ('matrix failure coincides with HE fibre failure'), and C_3 ('matrix failure coincides with the first LE fibre failure'). These curves divide the $(P_0/T_0, k_{\mathrm{HE}}/k_{\mathrm{LE}})$ parameter space into size 'zones', labelled $Z_1, Z_2, \ldots, Z_6$ in Fig. 10. The qualitative failure modes in each zone are tabulated in Tab. 1.

3.5 Fracture energy

Fracture energies are computed according to Sec. 2.10 at each point in the $(P_0/T_0, k_{\mathrm{HE}}/k_{\mathrm{LE}})$ space. Most notably, only those failure events that occur prior to the application of the maximum load on the model composite contribute to the fracture energy.

Fig. 11a shows the contour plot of the fracture energy, Δe (Eq. (78)) over the $(P_0/T_0, k_{\mathrm{HE}}/k_{\mathrm{LE}})$ parameter space. Clearly, Δe increases with increasing P_0/T_0 and with decreasing $k_{\mathrm{HE}}/k_{\mathrm{LE}}$. The largest values of Δe occur in zones Z_4 and Z_6. These values are orders of magnitude larger than the values obtained in any of the other zones. The Δe contours are continuous across the curve C_3. In both zones Z_4 and Z_6, LE fibre breaks and matrix failures occur before the fracture development becomes catastrophic with the failure of an HE fibre (Table 1). The continuity of the contour lines across C_3 shows that the order of first occurrence of these LE fibre failure and matrix failure is unimportant in these zones.

Fig. 11b shows the fracture energy associated with matrix failure, $\sum_\delta \Delta g_{m_{M_\delta}}$ (Eq. (78)) over the parameter space. For all $(P_0/T_0, k_{\mathrm{HE}}/k_{\mathrm{LE}})$ within zones Z_1 and Z_2, wherein there is no matrix failure, the fracture energy associated with matrix failure is zero; the small values in these zones seen in Fig. 11b are due to contour smoothing. Within zone Z_3, matrix failure occurs, but only after the fracture development has become catastrophic (Table 1). The matrix contribution is thus not included in the fracture energy computation, as detailed in Sec. 2.10. In zone Z_5, matrix failure contributes to the fracture energy, but this contribution is clearly very small, as seen in Fig. 11b. The largest contributions clearly only occur in zones Z_4 and Z_6. In Z_4, the matrix failure contribution to the fracture energy is nearly independent of P_0/T_0. In Z_6, there is a dependence on P_0/T_0, which becomes stronger with decreasing $k_{\mathrm{HE}}/k_{\mathrm{LE}}$. There is a discontinuity across the curve C_3 in the value of $\sum_\delta \Delta g_{m_{M_\delta}}$, which is smoothed out

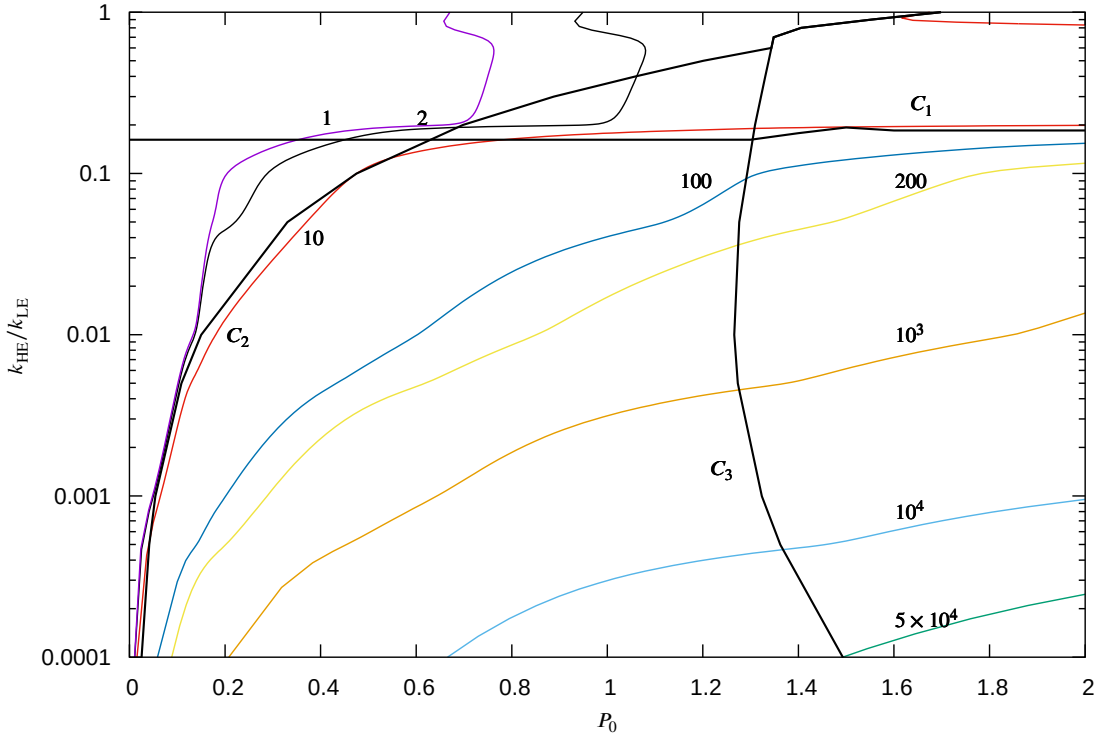

(a) Fracture energy, Δe. Maximum value = 8.98×10^4, at $(P_0/T_0, k_{HE}/k_{LE}) = (2, 0.0001)$.

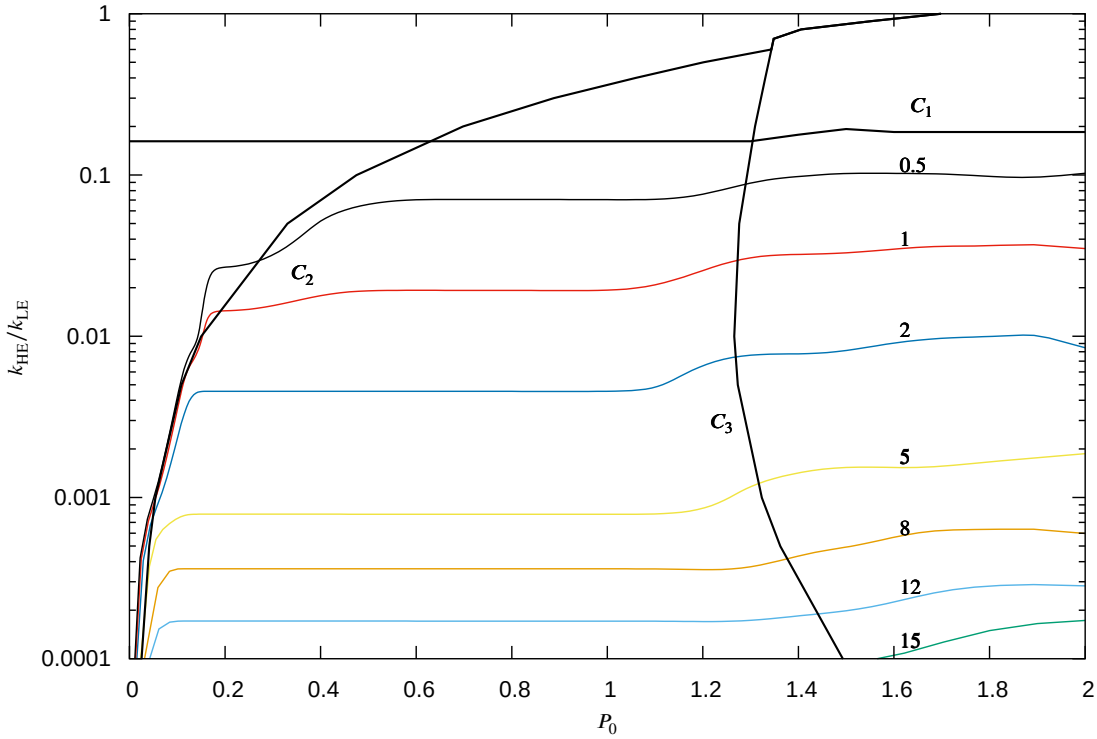

(b) Fracture energy associated with matrix failure events, $\sum_\delta \Delta g_{m_{M_\delta}}$. Maximum value = 18.3, at $(P_0/T_0, k_{HE}/k_{LE}) = (2, 0.0001)$.

Fig. 11: Variation of the (a) total fracture energy, Δe and (b) fracture energy contribution from matrix failure, $\sum_\delta \Delta g_{m_{M_\delta}}$, defined in Sec. 2.10 over the $(P_0/T_0, k_{HE}/k_{LE})$ parameter space. Also shown are the three curves C_1, C_2, and C_3 separating the six zones defined in Fig. 10.

in the course of contour plotting. This is because in zone Z_6, matrix failure initially occurs in a model composite with no LE fibre breaks and therefore greater stored strain energy, while in zone Z_4, matrix failure occurs in the presence of LE fibre breaks.

It is clear by comparing Figs. (11a) and (11b) that the contribution from matrix failure to the total fracture energy is very small. Indeed, $\sum_\delta \Delta g_{m_{M_\delta}}$ is seen to be orders of magnitude smaller than the total fracture energy, Δe. This shows that fibre failures predominantly contribute to the total fracture energy, i.e., $\Delta e \approx \sum_\beta \Delta g_{f_{F_\beta}}$ in Eq. (78).

Two counterparts of a hybrid composite corresponding to the parameter values $(P_0/T_0, k_{\mathrm{HE}}/k_{\mathrm{LE}})$ are now considered for comparison. The first is called the non-hybrid counterpart. The non-hybrid counterpart of a hybrid composite is obtained by setting $k_{\mathrm{HE}}/k_{\mathrm{LE}} = 1$, and keeping all other model parameters unchanged. Properties associated with the non-hybrid counterpart are indicated by the subscript "nh". The second is termed the perfect matrix counterpart. Matrix failure is disallowed in this counterpart by setting $T_0 = \infty$ in the hybrid composite, while keeping all other model parameters unchanged. Properties associated with the second counterpart are indicated by the subscript "pm".

In order to illuminate the role of fibre hybridisation, the fracture energy of each hybrid composite in the present parameter space is compared with that of its non-hybrid counterpart in Fig. 12a. Let Δe and Δe_{nh} denote the fracture energies of the hybrid composite, and non-hybrid counterpart, respectively. The contours of $\Delta e/\Delta e_{\mathrm{nh}}$ are shown in Fig. 12a. In zones Z_1, Z_3, and Z_5, $\Delta e/\Delta e_{\mathrm{nh}} \approx 1$. In zones Z_2, Z_4, and Z_6 $\Delta e/\Delta e_{\mathrm{nh}} > 1$ is obtained. This is because $p_{\mathrm{HE}} > p_{\mathrm{LE}}$ in these zones, and the HE fibre failure occurs in a condition of equal load sharing, after the failure of all LE fibres, as seen in Figs. 8c and 8e. The large values of $\Delta e/\Delta e_{\mathrm{nh}}$ suggests that the equal load sharing among HE fibres in a hybrid composite is an important reason for the enhancement of fracture energy.

In each of the parts of zone Z_6 corresponding to $P_0/T_0 < 1.7$, and to $P_0/T_0 > 1.7$, $\Delta e/\Delta e_{\mathrm{nh}}$ is nearly independent of P_0/T_0. In these regions, the increase in fracture energy due to hybridisation depends only on $k_{\mathrm{HE}}/k_{\mathrm{LE}}$, and increases with decreasing $k_{\mathrm{HE}}/k_{\mathrm{LE}}$. It does not depend on P_0/T_0. There is a step jump in $\Delta e/\Delta e_{\mathrm{nh}}$ across $P_0/T_0 = 1.7$, indicated by the vertical dotted line in Fig. 12a. This jump occurs because the non-hybrid counterpart fails without matrix failures for $P_0/T_0 < 1.7$, and undergoes matrix failure for $P_0/T_0 > 1.7$. This makes Δe_{nh} larger for $P_0/T_0 > 1.7$, and causes a jump in the ratio $\Delta e/\Delta e_{\mathrm{nh}}$. The step jump is smoothed over in the contour plot.

The importance of matrix failure is next examined by comparing the ratio of the fracture energy of the perfect matrix counterpart of the hybrid composite, with that of the non-hybrid counterpart, i.e., $\Delta e_{\mathrm{pm}}/\Delta e_{\mathrm{nh}}$ in Fig. 12b. In zones Z_1, Z_3, and Z_5, $\Delta e_{\mathrm{pm}}/\Delta e_{\mathrm{nh}} \leq 1$. In zones Z_2, Z_4, and Z_6, $\Delta e_{\mathrm{pm}}/\Delta e_{\mathrm{nh}}$ depends only on $k_{\mathrm{HE}}/k_{\mathrm{LE}}$, and not on P_0/T_0. This is because $T_0 = \infty$ in the pm counterpart, so that $P_0/T_0 = 0$ for all finite P_0. A step in $\Delta e_{\mathrm{pm}}/\Delta e_{\mathrm{nh}}$ occurs at $P_0/T_0 = 1.7$. The reason for this step is the same as given in connection with Fig. 12a above. Most significantly, comparing Figs. 12a and 12b shows that

$$\Delta e_{\mathrm{pm}}/\Delta e_{\mathrm{nh}} \ll \Delta e/\Delta e_{\mathrm{nh}}. \tag{85}$$

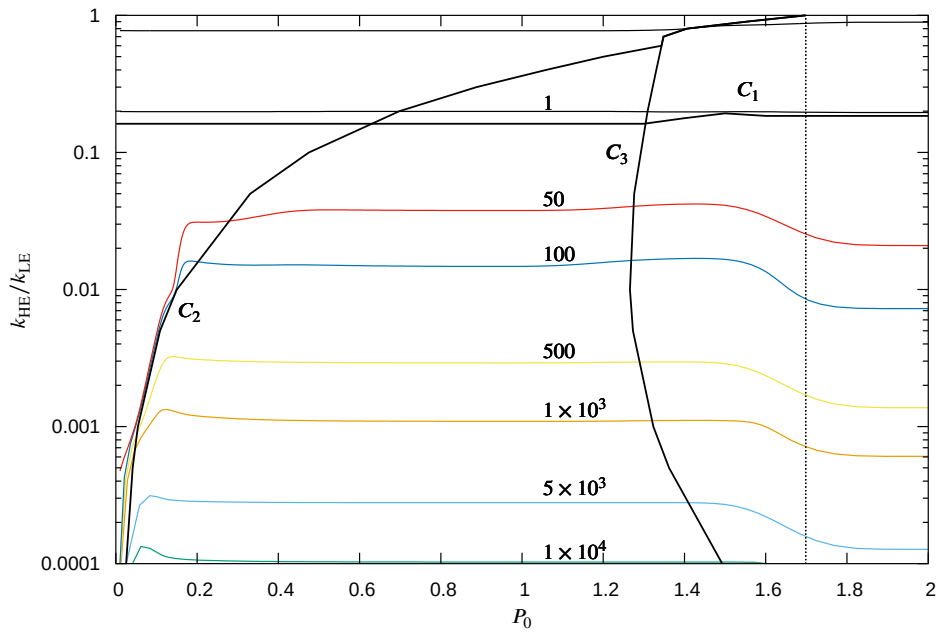

(a) Ratio of fracture energies of a hybrid composite and its non-hybrid counterpart, $\Delta e/\Delta e_{\mathrm{nh}}$. Maximum value = 1.28×10^4, at $(P_0/T_0, k_{\mathrm{HE}}/k_{\mathrm{LE}}) = (0.05, 0.0001)$.

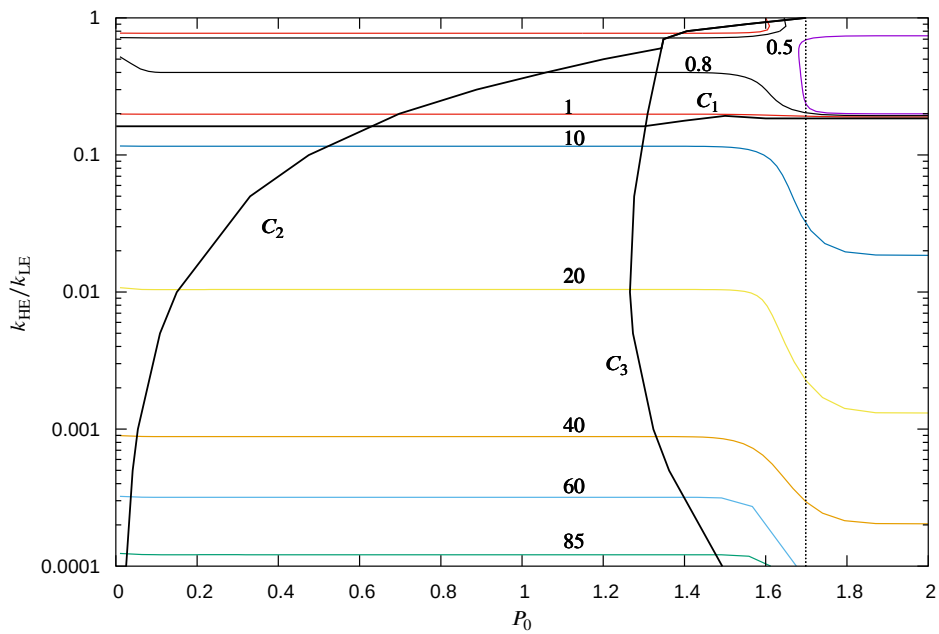

(b) Ratio of fracture energies of perfect matrix and non-hybrid counterparts of the composites, $\Delta e_{\mathrm{pm}}/\Delta e_{\mathrm{nh}}$. Maximum value = 90, achieved for $k_{\mathrm{HE}}/k_{\mathrm{LE}} = 0.0001$, and $P_0/T_0 \leq 1.7$.

Fig. 12: Fracture energy ratios demonstrating the role of (a) fibre hybridisation, and (b) matrix failure. Both effects are predominantly dependent only on $k_{\mathrm{HE}}/k_{\mathrm{LE}}$, and increase with decreasing $k_{\mathrm{HE}}/k_{\mathrm{LE}}$.

This shows that even though matrix failure entails a negligible amount of energy (Fig. 11b), it plays a crucial role in the development of fibre breakages, and thereby enhances the overall fracture energy of the hybrid composite. Further, it shows that the fibre hybridisation alone does not significantly enhance fracture energy if matrix failures are suppressed.

Thus, the role of matrix failure in enhancing the fracture toughness of the composite, and in producing the hybrid effect lies in altering the development of fibre breaks. This alteration can take one of two forms. First, as shown in Figs. 9e and 9f representing a typical point in zone Z_6, matrix failure can divert fibre failures away from a common transverse plane in the hybrid composite, producing large enhancements of the fracture energy over the non-hybrid and perfect matrix counterparts. Second, as shown in Figs. 8e and 8f representing a typical point in zone Z_4, fibre breaks may be confined to a transverse plane, but matrix failure reduces the stress concentrations in that plane (Fig. 6), to yield more modest enhancements in the fracture energy.

3.6 Fracture load

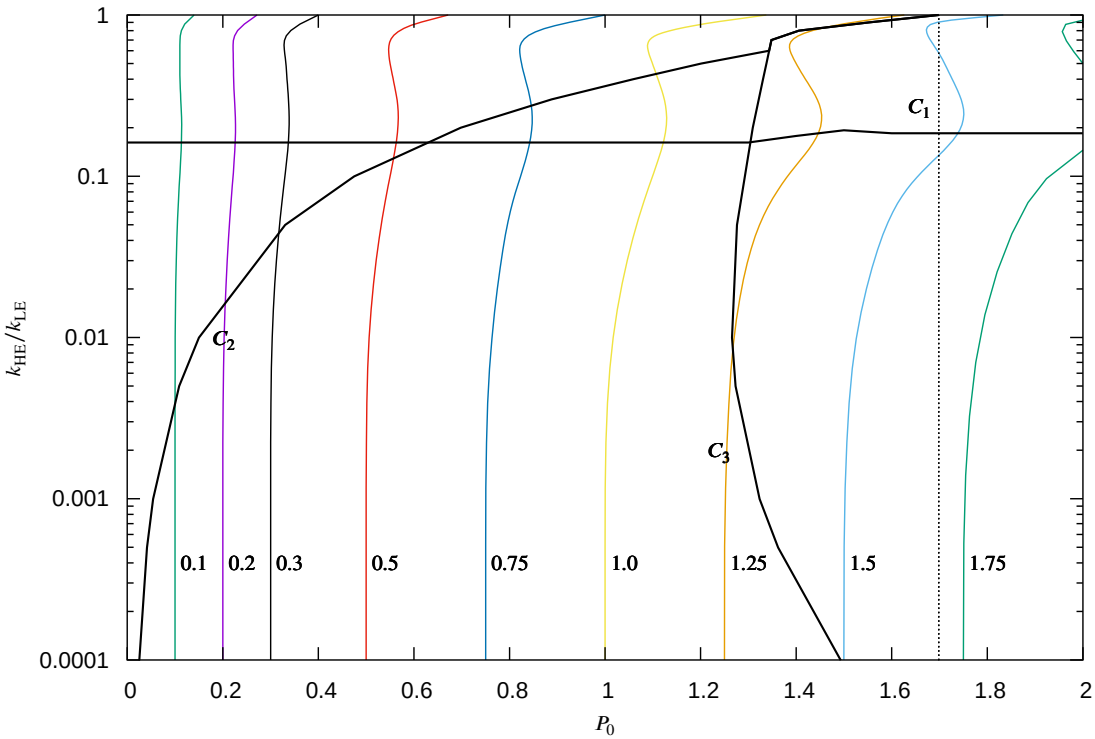

Fig. 13: Variation of the fracture load, p_{max}, over the $(P_0/T_0, k_{HE}/k_{LE})$ parameter space.

The far-field loads per fibre when the first LE and HE fibres break, were defined in Sec. 3.3, and are denoted p_{LE} and p_{HE}, respectively. The strength of the hybrid composite is then given by

$$p_{max} = \max\left\{p_{LE}, p_{HE}\right\}. \tag{86}$$

Fig. 13 shows the variation of $p_{\max}$ over the $(P_0/T_0, k_{\mathrm{HE}}/k_{\mathrm{LE}})$ parameter space. Most notably, for small $k_{\mathrm{HE}}/k_{\mathrm{LE}} \leq 0.01$, $p_{\max}$ is independent of $k_{\mathrm{HE}}/k_{\mathrm{LE}}$. Instead, $p_{\max}$ has a monotonic dependence on P_0/T_0. For larger $k_{\mathrm{HE}}/k_{\mathrm{LE}}$ also, $p_{\max}$ is nearly independent of $k_{\mathrm{HE}}/k_{\mathrm{LE}}$ for small $P_0/T_0 < 1$. It is only when both $k_{\mathrm{HE}}/k_{\mathrm{LE}} \geq 0.01$ and $P_0/T_0 \geq 1$ that $p_{\max}$ depends appreciably on both $k_{\mathrm{HE}}/k_{\mathrm{LE}}$ and P_0/T_0.

3.7 Fracture strain

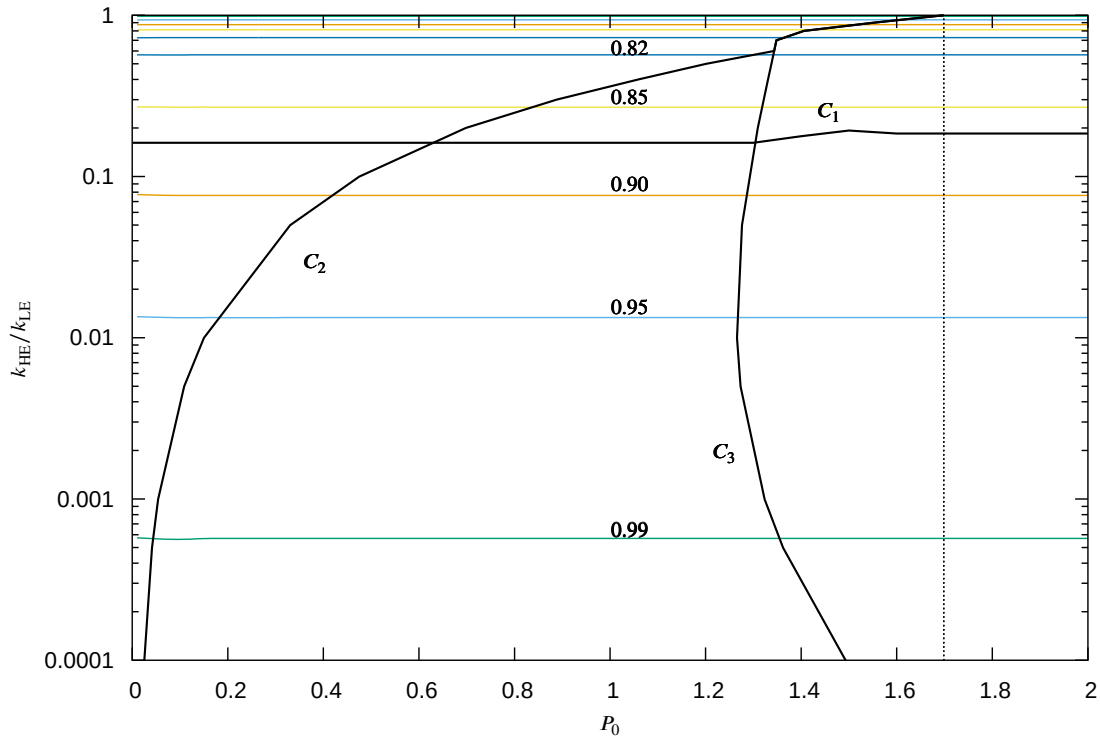

Fig. 14: Variation of the hybrid effect (Swolfs et al 2014) in composites with a perfect matrix ($T_0 = \infty$) over the $(P_0/T_0, k_{\mathrm{HE}}/k_{\mathrm{LE}})$ parameter space. The hybrid effect is the ratio of the far-field strain in a hybrid composite with a perfect matrix ($T_0 = \infty$) at the point of failure of the first LE fibre and the far-field strain in its non-hybrid counterpart, $\epsilon^{\mathrm{ff}}_{\mathrm{pm,LE}}/\epsilon^{\mathrm{ff}}_{\mathrm{pm,nh}}$.

It follows from Eq. (31) that for fixed k_0, p_∞ is proportional to the imposed far-field strain. Let $\epsilon^{\mathrm{ff}}_{\mathrm{LE}}$ denote the far-field strain in all the fibres at the instant at which the first LE fibre fails in the hybrid composite. Let $\epsilon^{\mathrm{ff}}_{\mathrm{pm,LE}}$ denote the far-field strain in the perfect matrix counterpart at the point of failure of the first LE fibre, defined in Sec. 3.5. The perfect matrix counterpart suffers no matrix failures ($T_0 = \infty$). Also, as in Sec. 3.5, let $\epsilon^{\mathrm{ff}}_{\mathrm{nh}}$ denote the far-field strain in the non-hybrid counterpart at the point of failure of the first fibre. In the non-hybrid counterpart, there is no distinction between LE and HE fibres, so the point of failure of the first LE fibre also corresponds to the point of catastrophic crack growth. Finally, let $\epsilon^{\mathrm{ff}}_{\mathrm{pm,nh}}$ denote the far-field strain in the perfect matrix, non-hybrid counterpart. This corresponds to $T_0 = \infty$, and $k_{\mathrm{HE}}/k_{\mathrm{LE}} = 1$, simultaneously.

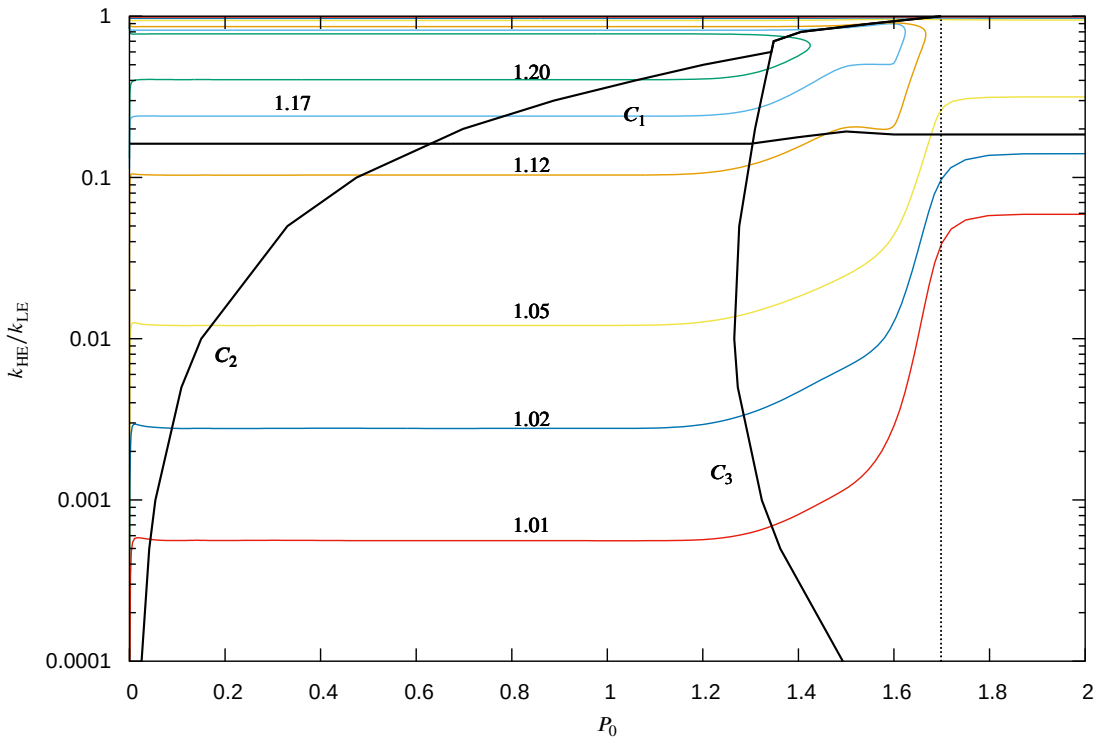

(a) Ratio of far-field strain in the hybrid composite, and in the non-hybrid counterpart, $\epsilon^{ff}_{LE}/\epsilon^{ff}_{nh}$ at the point of failure of the first LE fibre. Maximum value = 1.231 at $(P_0/T_0, k_{HE}/k_{LE}) = (0.05, 0.7)$.

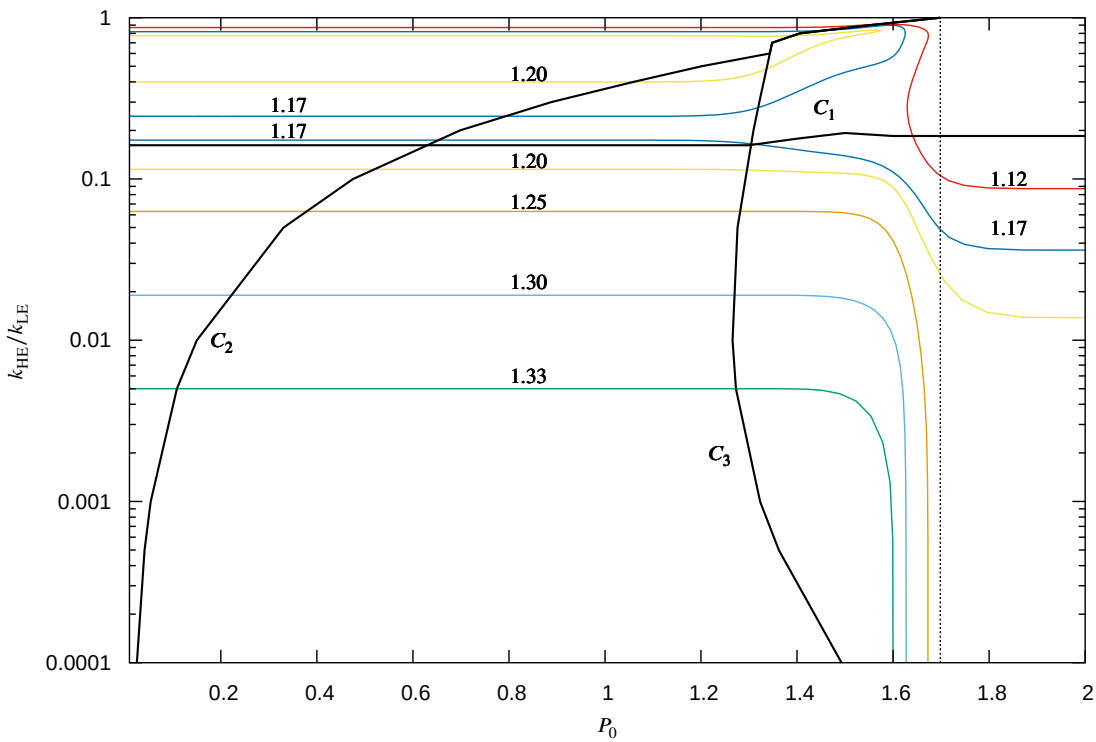

(b) Ratio of far-field strain in the hybrid composite, and in the non-hybrid counterpart, $\epsilon^{ff}_{max}/\epsilon^{ff}_{nh}$ at the point of initiation of catastrophic crack growth. Maximum value = 1.334 at $(P_0/T_0, k_{HE}/k_{LE}) = (0.05, 0.0001)$.

Fig. 15: Variation of the hybrid effect, (a) h_{LE} (Eq. 87), and (b) h_{max} (Eq. 88), over the $(P_0/T_0, k_{HE}/k_{LE})$ parameter space.

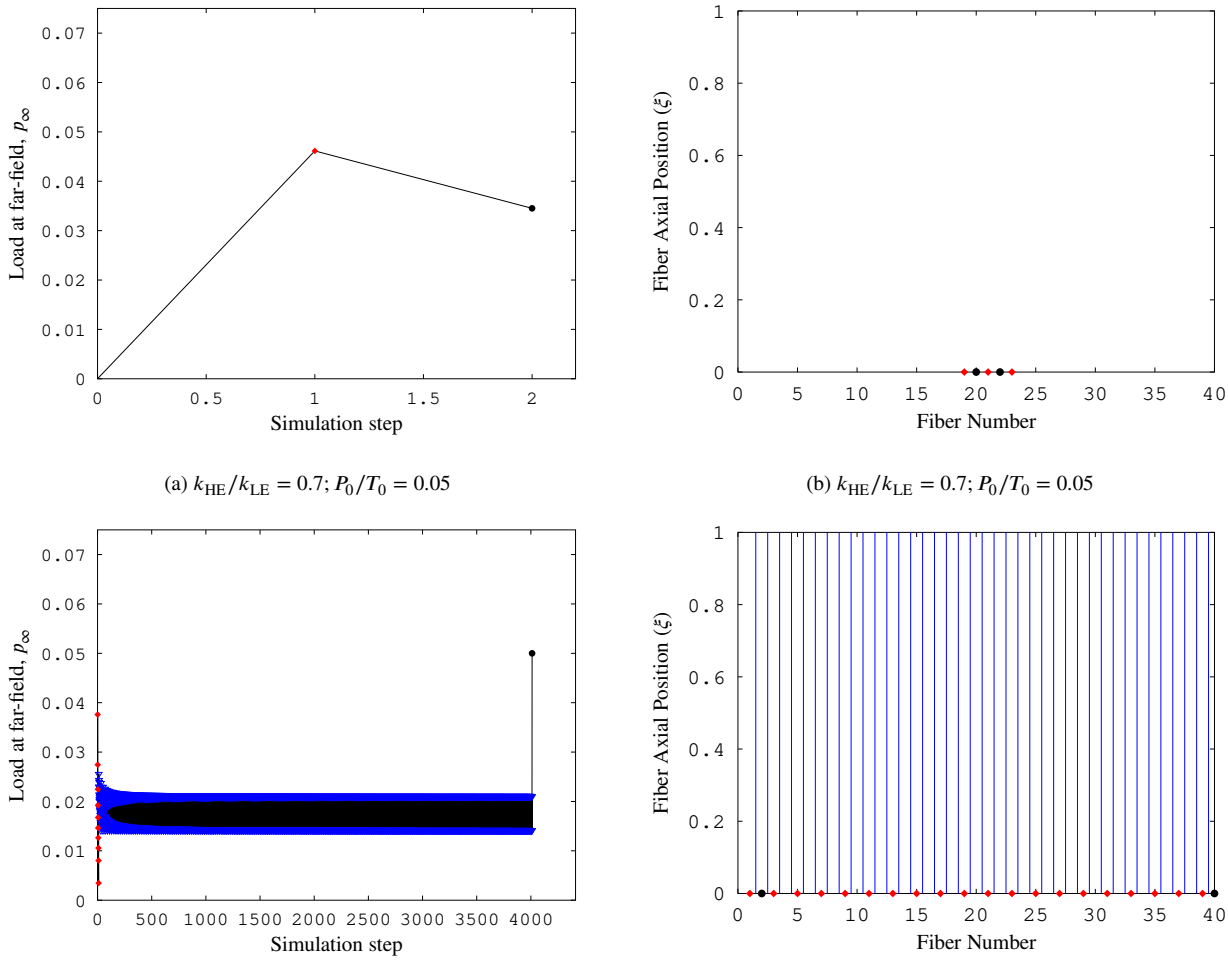

(a) $k_{\mathrm{HE}}/k_{\mathrm{LE}} = 0.7$; $P_0/T_0 = 0.05$

(b) $k_{\mathrm{HE}}/k_{\mathrm{LE}} = 0.7$; $P_0/T_0 = 0.05$

(c) $k_{\mathrm{HE}}/k_{\mathrm{LE}} = 0.0001$; $P_0/T_0 = 0.05$

(d) $k_{\mathrm{HE}}/k_{\mathrm{LE}} = 0.0001$; $P_0/T_0 = 0.05$

Fig. 16: (a, c) Evolution of far-field load up to the point of breakage of an HE fibre. (b, d) Partially fractured state immediately after the HE fibre break. (a, b) correspond to the maximal value of the hybrid effect in Fig. 15a, and (c, d) to the maximal value in Fig. 15b. ◆ indicates LE fibre breaks, ● indicates HE fibre breaks, and ▽ and — indicate matrix failures.

The variation of $\epsilon^{\mathrm{ff}}_{\mathrm{pm,LE}}/\epsilon^{\mathrm{ff}}_{\mathrm{pm,nh}}$ over the $(P_0/T_0, k_{\mathrm{HE}}/k_{\mathrm{LE}})$ parameter space is shown in Fig. 14. Since $T_0 = \infty$, $P_0/T_0 = 0$ for all finite P_0, and $\epsilon^{\mathrm{ff}}_{\mathrm{pm,LE}}/\epsilon^{\mathrm{ff}}_{\mathrm{pm,nh}}$ does not depend at all on P_0. It depends only on $k_{\mathrm{HE}}/k_{\mathrm{LE}}$. In a composite without matrix failure, $\epsilon^{\mathrm{ff}}_{\mathrm{pm,LE}}/\epsilon^{\mathrm{ff}}_{\mathrm{pm,nh}}$ is the hybrid effect, following the definition of Swolfs et al (2014). It is seen from Fig. 14 that a positive hybrid effect, i.e., $\epsilon^{\mathrm{ff}}_{\mathrm{pm}}/\epsilon^{\mathrm{ff}}_{\mathrm{pm,nh}} > 1$ is not possible anywhere within the $(P_0/T_0, k_{\mathrm{HE}}/k_{\mathrm{LE}})$ parameter space in a hybrid composite without matrix failure. This result is originally due to Fukunaga et al (1984).

Attention is next turned to the case where matrix failures are permitted, i.e., $T_0 = 1$. The variation of the ratio,

$$h_{\mathrm{LE}} = \epsilon^{\mathrm{ff}}_{\mathrm{LE}}/\epsilon^{\mathrm{ff}}_{\mathrm{nh}}, \tag{87}$$

which can be regarded as the hybrid effect in such composites (Swolfs et al 2014), over the $(P_0/T_0, k_{\mathrm{HE}}/k_{\mathrm{LE}})$ parameter space is shown in Fig. 15a. The greatest hybrid effect of $h_{\mathrm{LE}} = \epsilon^{\mathrm{ff}}_{\mathrm{LE}}/\epsilon^{\mathrm{ff}}_{\mathrm{nh}} = 1.23$ is realised at $(P_0/T_0, k_{\mathrm{HE}}/k_{\mathrm{LE}}) = (0.05, 0.7)$. This is comparable to the measurements of the hybrid effect in various hybrid composites, as reported in the literature, and collated by

Swolfs et al (2014, Table 1). The evolution of p_∞ and fracture state at the point of failure of the first HE fibre in this maximal specimen are shown in Figs. 16a, and 16b, respectively.

The predicted maximal hybrid effect, 23%, is comparable to the measurements of the hybrid effect reported in the literature by Wisnom et al (2016), who reported an experimental value of 18% in a carbon/glass/epoxy system. The present observation, together with that in Fig. 12a show that parameters for which the maximal hybrid effect and the maximal fracture energy are realised are very different. In particular, the maximal hybrid effect requires $k_{\mathrm{HE}}/k_{\mathrm{LE}} \approx 0.5$, while maximising the fracture energy ratio requires a vanishingly small $k_{\mathrm{HE}}/k_{\mathrm{LE}}$.

Let $\epsilon^{\mathrm{ff}}_{\mathrm{max}}$ denote the far-field strain in all the fibres at the instant of initiation of catastrophic crack growth in the hybrid composite. The far-field load at this point is given by p_{max} defined in Eq. (86). The variation of

$$h_{\mathrm{max}} = \epsilon^{\mathrm{ff}}_{\mathrm{max}}/\epsilon^{\mathrm{ff}}_{\mathrm{nh}}, \tag{88}$$

over the $(P_0/T_0, k_{\mathrm{HE}}/k_{\mathrm{LE}})$ space is shown in Fig. 15b. In zones Z_1, Z_3, and Z_5, catastrophic fracture initiates with the failure of an LE fibre. The contours of h_{max} shown in Fig. 15b coincide with those shown in Fig. 15a in these zones. However, in zones Z_2, Z_4, and Z_6, values of $\epsilon^{\mathrm{ff}}_{\mathrm{max}}/\epsilon^{\mathrm{ff}}_{\mathrm{nh}}$ larger than in zones Z_1, Z_3, and Z_5 are realised. In fact, the largest $h_{\mathrm{max}} = 1.334$ occurs at small values of $k_{\mathrm{HE}}/k_{\mathrm{LE}}$ in zone Z_4. The evolution of p_∞ and fracture state at the end of the simulation in this maximal specimen are shown in Figs. 16c, and 16d, respectively. Extensive matrix failure is observed. The parametric region where $\epsilon^{\mathrm{ff}}_{\mathrm{max}}/\epsilon^{\mathrm{ff}}_{\mathrm{nh}}$ is maximised coincides with the region where the ratio $\Delta e/\Delta e_{\mathrm{nh}}$ is maximised, as seen from Fig. 12a.

3.8 Summary

The magnitudes of the fracture energy, and that of failure strain or load, increase monotonically with fibre strength, P_0/T_0. Therefore, a strong and tough hybrid composite should combine large P_0/T_0 with small $k_{\mathrm{HE}}/k_{\mathrm{LE}}$. Efforts to enhance the hybrid effect, Eq. (87), discussed extensively in the literature (Swolfs et al 2014) amount to enhancing the strain at which the first LE fibre breaks, by introducing HE fibres. A notable conclusion from the present analysis is that neither does maximising the hybrid effect serve to maximise the fracture energy and ultimate tensile strain, nor vice-versa.

4 Discussion

It is generally believed (Manders and Bader 1981; Fukunaga et al 1984; Swolfs et al 2014) that the hybrid effect can only arise if the LE fibres have non-deterministic strengths. These works did not account for matrix failure. The present work shows that when matrix failure is accounted for, a significant hybrid effect is possible, even with uniform deterministic strengths of all tensile elements. The present work also shows that matrix failure accounts for a very small fraction of the composite fracture energy. Nevertheless, the role of matrix failure in enhancing the fracture toughness of the composite, and in producing the hybrid effect lies in altering the development of fibre breaks.

The present results are now revisited in the context of two material systems mentioned in Sec. 1, viz., double network hydrogels, and hybrid carbon/glass/epoxy composites.

4.1 Double Network Hydrogels

Double network hydrogels are soft and wet polymer gels comprised of two types of polymer networks and water. Gong et al (2003) studied hydrogels of polymerised PAMPS, and polymerised PAAm. They observed that these gels are of comparable strength and toughness. They also reported that when a highly cross-linked PAMPS gel is swollen in a solution of PAAm, and polymerised, the resulting gel is of the order of 1000 times tougher than either the PAMPS or PAAm gels. The interaction between the two networks is through entanglement of their strands, and some covalent bonding (Tsukeshiba et al 2005; Nakajima et al 2009).

In tearing tests of double network hydrogels with a pre-existing notch, Yu et al (2009) reported direct observation under ultraviolet light of transverse material damage ahead of the progressing crack tip. They also reported longitudinal material damage extending a finite distance to either side of the fracture plane. Gong (2010) attributed the observed material damage to the failure of the stiff PAMPS strands, which she termed 'sacrificial bonds' bridged by strands of the much more flexible PAAm network.

In the context of the present model, the LE and HE fibres represent the strands of the PAMPS and PAAm networks approximately aligned with the tensile direction. The matrix represents the strands of the PAMPS network aligned approximately transverse to the loading direction. It is reasonable to expect that the polymeric strands aligned with the tensile direction will predominantly be loaded in tension, and those aligned with the transverse direction will be mostly loaded in shear. Intense cross-linking makes the PAMPS network highly stiff; the relatively smaller intensity of cross-linking makes the PAAm network much more flexible (Rubinstein and Colby 2003). In the model hydrogel, therefore, $k_{\mathrm{HE}}/k_{\mathrm{LE}} \ll 1$. Also, the assumption of the model that both LE and HE fibres have similar tensile strengths is satisfied reasonably by the physical hydrogel (Gong et al 2003). In an isotropic hydrogel network, under plane stress, a state of pure shear stress corresponds to a principal stress whose magnitude equals the shear stress. Since in the double network hydrogel, the same PAMPS network serves as both LE fibres, and matrix, it is reasonable to assume that P_0/T_0 is of the order of unity.

$P_0/T_0 \approx 1$, and $k_{\mathrm{HE}}/k_{\mathrm{LE}} \ll 1$ puts the double network hydrogel within zone Z_4 in Fig. 10. Very large fracture energy enhancements are predicted in zone Z_4 (Fig. 12a), which are comparable to the fracture energy enhancements of the order of 10^3 reported by Gong et al (2003); Tsukeshiba et al (2005), and Nakajima et al (2009). Gong et al (2003) also reported enhancement of the fracture strain, $\epsilon_{f_{\mathrm{i}},\mathrm{max}}(\xi = \pm\infty)/\epsilon_{f_{\mathrm{i}},\mathrm{nh}}(\xi = \pm\infty)$ of about 2. The present model predicts about $\epsilon_{f_{\mathrm{i}},\mathrm{max}}(\xi = \pm\infty)/\epsilon_{f_{\mathrm{i}},\mathrm{nh}}(\xi = \pm\infty) \approx 1.33$. This underestimation is likely because the physical material has a highly non-linear constitutive response, which is not captured by the present linear elastic model.

4.2 Carbon/glass epoxy hybrid composites

A number of works in the literature report studies on interlayer carbon/glass/epoxy composites (Bunsell and Harris 1974; Aveston and Sillwood 1976; Manders 1979; Wisnom et al 2016; Czél and Wisnom 2013). These composites are comprised of carbon and glass plies in epoxy resin bonded together. As the carbon and glass fibres in these studies are not intermingled as in the model, quantitative comparisons with the results reported in these works is difficult.

However, You et al (2007) studied the failure of 3D intrayarn carbon/glass/vinylester and polyester composite rods. While their 3D specimen geometry differs from the 2D geometry of the present model, the carbon and glass fibres were intermingled in the specimen of You et al (2007), just as in the present model. Using the material data presented by You et al (2007), for LE carbon and HE glass fibres, $k_{\mathrm{HE}}/k_{\mathrm{LE}} \approx 0.3$, $P_0 = 0.17$ N using Eq. (63), and $T_0 = 0.016$ N, using Eq. (64). Thus, $P_0/T_0 \approx 10$. The point $(P_0/T_0, k_{\mathrm{HE}}/k_{\mathrm{LE}})$ falls within zone Z_5; here, much matrix debonding is observed, but $p_{\mathrm{HE}} < p_{LE}$. This prediction agrees with the experimental observation of You et al (2007, Fig. 2 (e), (f)). Also, You et al (2007) measured ultimate tensile strain enhancements of 1.33, and 1.14 for the vinyl ester and polyester matrix rods. From Fig. 15b, $\epsilon_{f_{\mathrm{i}},\mathrm{max}}(\xi = \pm\infty)/\epsilon_{f_{\mathrm{i}},\mathrm{nh}}(\xi = \pm\infty) < 1.12$ at $(P_0/T_0, k_{\mathrm{HE}}/k_{\mathrm{LE}}) \approx (10, 0.3)$. Thus, while the present model predicts an enhancement of the failure strain in qualitative agreement with the experimental observations, it does not quantitatively match the failure strain enhancement. This likely arises because the physical specimen is 3-dimensional, while the model specimen is 2-dimensional. The stress concentrations surrounding fibre breaks in the 2-dimensional model will overestimate the stress concentrations in the physical 3-dimensional specimen.

5 Conclusions

A linear elastic shear-lag model is developed for unidirectional hybrid fibre composite lamina with alternating low extension (LE) and high extension (HE) fibres embedded in matrix. Fibre breakage, and matrix failure are the two microscopic fracture mechanisms accounted for in this study. Fibre strengths are assumed deterministic, and the LE and HE fibres are assumed equally strong. The effect of two parameters, viz., stiffness contrast of the fibres, $k_{\mathrm{HE}}/k_{\mathrm{LE}}$, and the ratio of the fibre strengths in tension to shear strength of the matrix, P_0/T_0, on fracture development, fracture energy, and fracture strain have been systematically investigated through computer simulations of fracture that implement the shear-lag model. Curves have been identified in the two-dimensional $(k_{\mathrm{HE}}/k_{\mathrm{LE}}, P_0/T_0)$ parametric space that separate it into regions of matrix failure and matrix non-failure, and that separate it into regions of catastrophic crack growth after the failure of an LE fibre and catastrophic crack growth after the failure of an HE fibre. The largest fracture energies are found associated with $k_{\mathrm{HE}}/k_{\mathrm{LE}} \downarrow 0$. The largest hybrid effect (Swolfs et al 2014) is associated with $k_{\mathrm{HE}}/k_{\mathrm{LE}} \approx 0.7$.

The present model can qualitatively explain the enormous enhancement of the fracture toughness of double network hydrogels over their single network counterparts. It also qualitatively explains the parameter regime, identified in the literature through experiments (Gong et al 2003; Tsukeshiba et al 2005; Nakajima et al 2009), wherein the hybrid effect is maximised. The present

results also show that composite parameters maximising the hybrid effect and those maximising the fracture toughness are very different. In fact, parameters that maximise the hybrid effect result correspond to rather low fracture energies.

The present study has a number of limitations: (1) Simulations have been made in patches with only 40 fibres for computational tractability. The observed fracture modes may be somewhat modified if larger patches could be simulated. New algorithms and/or more computational resources may be needed to address this limitation. (2) Matrix failure has been assumed to occur due to shear stresses alone. In general though, tensile stresses in the direction transverse to the fibres may be important to realistically model matrix splitting (Goree and Gross 1980; Dharani et al 1983), which can only be captured with a two-dimensional model. A computationally light two-dimensional model is needed to address this limitation. (3) The material response of all the phases of the present material has been assumed linear elastic. This is evidently inappropriate when the model is applied to soft hydrogels. An extension of the present model to non-linear material responses is needed (Ogden 1997). (4) Realistic composites are often 3D in shape. Stress concentrations are substantially smaller in 3D than in 2D. An extension of the present study to 3D composites is therefore needed. (5) LE and HE fibres have been assumed to alternate in the present model. Physically, fibre arrangements and volume fractions could be much more complex (Swolfs et al 2014). (6) While the strengths of the LE and HE fibres are typically similar (Jawaid and Khalil 2011), in the present work, they have been assumed equal. A study of the effects of variation in the strengths of the LE and HE fibres is needed. (7) LE and HE fibres diameters have been assumed equal. This need not be the case in general (Fidelis et al 2013), and must be accounted for. (8) Randomness in the fibre strengths has been ignored presently (Zweben 1977). While limitations (1)–(3) need the development of new tools and techniques to overcome, limitations (4)–(8) can be adequately addressed already using the present tools. These studies will be reported in future work.

6 Acknowledgements

The authors gratefully acknowledge use of the High Performance Computing Environment (HPCE) at the P. G. Senapathy Centre for Computing Resources, IIT Madras, for conducting the simulations reported in this work.

References

Aveston J, Sillwood J (1976) Synergistic fibre strengthening in hybrid composites. Journal of Materials Science 11(10):1877–1883

Beyerlein IJ, Phoenix SL, Sastry AM (1996) Comparison of shear-lag theory and continuum fracture mechanics for modeling fiber and matrix stresses in an elastic cracked composite lamina. International Journal of Solids and Structures 33(18):2543–2574

Brown HR (2007) A model of the fracture of double network gels. Macromolecules 40(10):3815–3818

Bunsell A, Harris B (1974) Hybrid carbon and glass fibre composites. Composites 5(4):157–164

Cox H (1952) The elasticity and strength of paper and other fibrous materials. British journal of applied physics 3(3):72

Czél G, Wisnom M (2013) Demonstration of pseudo-ductility in high performance glass/epoxy composites by hybridisation with thin-ply carbon prepreg. Composites Part A: Applied Science and Manufacturing 52:23–30

Dharani LR, Recker RL (1991) Growth of longitudinal matrix damage in unidirectional composites. Engineering fracture mechanics 38(2):185–195

Dharani LR, Jones WF, Goree JG (1983) Mathematical modeling of damage in unidirectional composites. Engineering Fracture Mechanics 17(6):555–573

Fidelis MEA, Pereira TVC, Gomes OdFM, de Andrade Silva F, Toledo Filho RD (2013) The effect of fiber morphology on the tensile strength of natural fibers. Journal of Materials Research and Technology 2(2):149–157

Fukuda H, Chou TW (1982) Monte carlo simulation of the strength of hybrid composites. Journal of Composite Materials 16(5):371–385

Fukunaga H, Chou TW, Fukuda H (1984) Strength of intermingled hybrid composites. Journal of reinforced plastics and composites 3(2):145–160

Gong JP (2010) Why are double network hydrogels so tough? Soft Matter 6(12):2583–2590

Gong JP, Katsuyama Y, Kurokawa T, Osada Y (2003) Double-network hydrogels with extremely high mechanical strength. Advanced Materials 15(14):1155–1158

Goree JG, Gross RS (1980) Analysis of a unidirectional composite containing broken fibers and matrix damage. Engineering Fracture Mechanics 13(3):563–578

Gücer D, Gurland J (1962) Comparison of the statistics of two fracture modes. Journal of the Mechanics and Physics of Solids 10(4):365–373

Harlow D (1983) Statistical properties of hybrid composites. i. recursion analysis. Proceedings of the Royal Society of London A: Mathematical, Physical and Engineering Sciences 389(1796):67–100

Hayashi T (1972) On the improvement of mechanical properties of composites by hybrid composition. In: Proc. 8th Intl. Reinforced Plastics Conf., pp 149–152

Hedgepeth JM (1961) Stress concentrations in filamentary structures. Tech. Rep. RN D-882, NASA

Jawaid M, Khalil HA (2011) Cellulosic/synthetic fibre reinforced polymer hybrid composites: A review. Carbohydrate Polymers 86(1):1–18

Kanninen M, Popelar C (1985) Advanced Fracture Mechanics. Oxford engineering science series, Oxford University Press

Karger-Kocsis J, Mahmood H, Pegoretti A (2015) Recent advances in fiber/matrix interphase engineering for polymer composites. Progress in Materials Science 73:1–43

Kim JK, Mai Yw (1991) High strength, high fracture toughness fibre composites with interface control—a review. Composites Science and Technology 41(4):333–378

Landis CM, Beyerlein IJ, McMeeking RM (2000) Micromechanical simulation of the failure of fiber reinforced composites. Journal of the Mechanics and Physics of Solids 48(3):621–648

Mahesh S, Phoenix S (2004) Lifetime distributions for unidirectional fibrous composites under creep-rupture loading. International Journal of Fracture 127(4):303–360

Manders P, Bader M (1981) The strength of hybrid glass/carbon fibre composites. Journal of materials science 16(8):2233–2245

Manders PW (1979) The strength of mixed fibre compostes. PhD thesis, University of Surrey, Surrey, UK

Nakajima T, Hidemitsu F, Yoshimi T, Takayuki K, Yoshihito O, Jian PG (2009) True chemical structure of double network hydrogels. Macromolecules 42(6):2184–2189

Ogden RW (1997) Non-linear elastic deformations. Courier Corporation

Phillips M (1981) Composition parameters for hybrid composite materials. Composites 12(2):113–116

Rosen BW (1964) Tensile failure of fibrous composites. AIAA j 2(11):1985–1991

Rubinstein M, Colby RH (2003) Polymer physics, vol 23. Oxford university press New York

Sharma M, Gao S, Mäder E, Sharma H, Wei LY, Bijwe J (2014) Carbon fiber surfaces and composite interphases. Composites Science and Technology 102:35–50

Swolfs Y, Gorbatikh L, Verpoest I (2014) Fibre hybridisation in polymer composites: a review. Composites Part A: Applied Science and Manufacturing 67:181–200

Tanaka Y (2007) A local damage model for anomalous high toughness of double-network gels. EPL (Europhysics Letters) 78(5):56,005

Tsukeshiba H, Huang M, Na YH, Kurokawa T, Kuwabara R, Tanaka Y, Furukawa H, Osada Y, Gong JP (2005) Effect of polymer entanglement on the toughening of double network hydrogels. The Journal of Physical Chemistry B 109(34):16,304–16,309

Weibull W (1952) A statistical distribution function of wide applicability. Journal of Applied Mechanics-Transactions of the ASME 19(2):233–234

Wisnom MR, Czél G, Swolfs Y, Jalalvand M, Gorbatikh L, Verpoest I (2016) Hybrid effects in thin ply carbon/glass unidirectional laminates: accurate experimental determination and prediction. Composites Part A: Applied Science and Manufacturing 88:131–139

You YJ, Park YH, Kim HY, Park JS (2007) Hybrid effect on tensile properties of frp rods with various material compositions. Composite structures 80(1):117–122

Yu QM, Tanaka Y, Furukawa H, Kurokawa T, Gong JP (2009) Direct observation of damage zone around crack tips in double-network gels. Macromolecules 42(12):3852–3855

Zweben C (1977) Tensile strength of hybrid composites. Journal of Materials Science 12(7):1325–1337